

Shedding the envelope: JWST reveals a kiloparsec-scale [OIII]-weak Balmer shell around a z=7.64 quasar

Julien Wolf¹, Eduardo Bañados¹, Xiaohui Fan², Antoine Dumont¹, James E. Davies¹, David S. N. Rupke^{3,4}, Jinyi Yang⁵, Weizhe Liu², Silvia Belladitta¹, Aaron Barth⁶, Sarah Bosman^{1,7}, Tiago Costa⁸, Frederick B. Davies¹, Roberto Decarli⁸, Dominika Ďurovčíková¹⁰, Anna-Christina Eilers¹⁰, Hyunsung D. Jun^{11,12}, Yichen Liu², Federica Loiacono⁹, Alessandro Lupi^{13,14,8}, Chiara Mazzucchelli¹⁵, Maria Pudoka², Sofia Rojas¹⁶, Jan-Torge Schindler¹⁷, Wei Leong Tee², Benny Trakhtenbrot¹⁸, Fabian Walter¹, Huanian Zhang¹⁹

¹ Max-Planck-Institut für Astronomie, Königstuhl 17, D-69117 Heidelberg, Germany

² Steward Observatory, University of Arizona, 933 N. Cherry Ave, Tucson, AZ 85719, USA

³ Department of Physics, Rhodes College, 2000 North Parkway, Memphis, TN 38112, USA

⁴ Zentrum für Astronomie der Universität Heidelberg, Astronomisches Rechen-Institut, Mönchhofstr 12-14, D-69120 Heidelberg, Germany

⁵ Department of Astronomy, University of Michigan, 1085 S. University Ave., Ann Arbor, MI 48109, USA

⁶ Department of Physics and Astronomy, University of California, Irvine, 4129 Frederick Reines Hall, Irvine, CA 92697-4575, USA

⁷ Institute for Theoretical Physics, Heidelberg University, Philosophenweg 12, D-69120 Heidelberg, Germany

⁸ School of Mathematics, Statistics and Physics, Newcastle University, Newcastle upon Tyne, NE1 7RU, UK

⁹ INAF – Osservatorio di Astrofisica e Scienza dello Spazio di Bologna, Via Gobetti 93/3, I-40129 Bologna, Italy

¹⁰ MIT Kavli Institute for Astrophysics and Space Research, 77 Massachusetts Avenue, Cambridge, MA 02139, USA

¹¹ Department of Physics, Northwestern College, 101 7th St SW, Orange City, IA 51041, USA

¹² School of Physics, Korea Institute for Advanced Study, 85 Hoegiro, Dongdaemun-gu, Seoul 02455, Republic of Korea

¹³ Como Lake Center for Astrophysics, DiSAT, Università degli Studi dell’Insubria, via Valleggio 11, I-22100, Como, Italy

¹⁴ INFN, Sezione Milano-Bicocca, P.zza della Scienza 3, I-20126 Milano, Italy

¹⁵ Instituto de Estudios Astrofísicos, Facultad de Ingeniería y Ciencias, Universidad Diego Portales, Avenida Ejercito Libertador 441, Santiago, Chile

¹⁶ Department of Physics and Astronomy, University of California, Los Angeles, 430 Portola Plaza, Los Angeles, CA 90095, USA

¹⁷ Hamburg Observatory, Gojenbergsweg 112, D-21029 Hamburg, Germany

¹⁸ School of Physics and Astronomy, Tel Aviv University, Tel Aviv 69978, Israel

¹⁹ Department of Astronomy, School of Physics, Huazhong University of Science and Technology, Luoyu Road, Wuhan, 430074, Hubei, China

Received October 31, 2025; accepted XXXX YY, 202Z

ABSTRACT

Luminous quasars at the redshift frontier $z > 7$ serve as stringent probes of super-massive black hole (SMBH) formation and they are thought to undergo much of their growth obscured by dense gas and dust in their host galaxies. Fully characterizing the symbiotic evolution of SMBHs and hosts requires rest-frame optical observations that span spatial scales from the broad-line region (BLR) to the interstellar and circumgalactic medium (ISM/CGM). The James Webb Space Telescope (JWST) now provides the necessary spatially resolved spectroscopy to do so. But the physical conditions that regulate the interplay between SMBHs and their hosts at the highest redshifts, especially the nature of early feedback phases, remain unclear. We present JWST/NIRSpec Integral Field Unit (IFU) observations of J0313-1806 at $z = 7.64$, the most distant luminous quasar known. From the restframe optical spectrum of the unresolved quasar, we derive a black hole mass of $M_{\text{BH}} = (1.63 \pm 0.10) \times 10^9 M_{\odot}$ based on $H\beta$ $\lambda 4861$ ($H\beta$) and an Eddington rate of $\lambda = L/L_{\text{Edd}} = 0.80 \pm 0.05$, consistent with previous $\text{Mg II} \lambda 2800$ -based estimates. J0313-1806 exhibits no detectable $[\text{O III}] \lambda\lambda 4959, 5007$ emission on nuclear scales (3σ upper limit equivalent width of $[\text{O III}] \lambda 5007 < 1.42 \text{ \AA}$). Most remarkably, we detect an ionized gas shell extending out to ~ 1.8 kpc traced by $H\beta$ emission that also lacks any significant $[\text{O III}] \lambda\lambda 4959, 5007$, with a 3σ upper limit on the $[\text{O III}] \lambda 5007$ to $H\beta$ flux ratio of $\log_{10}(F([\text{O III}]/F(H\beta))) = -1.15$. Through photoionization modelling, we demonstrate that the extended emission is consistent with a thin, clumpy outflowing shell where $[\text{O III}]$ is collisionally de-excited by dense gas. We interpret this structure as a fossil remnant of a recent blowout phase, providing evidence for episodic feedback cycles in one of the earliest quasars. These findings suggest that dense ISM phases may play a crucial role in shaping the spectral properties of quasars across cosmic time.

Key words. Galaxies: high-redshift; quasars: individual: J0313-1806; quasars: supermassive black holes

1. Introduction

In the luminous quasar phase, the powerful panchromatic radiation of active galactic nuclei (AGN) unambiguously traces the

accretion of a supermassive black hole (SMBH) at the centre of galaxies. Through dedicated optical and near-infrared (NIR) surveys, quasars have been discovered at ever increasing redshifts, well within the first gigayear of the Universe ($z > 5.6$, e.g., Fan et al. 2001; Reed et al. 2015; Wu et al. 2015; Bañados et al. 2016, 2023; Jiang et al. 2016; Matsuoka et al. 2016, 2018a,b; Matsuoka et al. 2019; Matsuoka et al. 2022, 2025; Wang et al. 2017; Gloudemans et al. 2022; Wolf et al. 2024; Ighina et al. 2024; Belladitta et al. 2025). The SMBHs powering these distant quasars populate the extreme end of the black hole mass scale ($10^8 - 10^{10} M_\odot$, e.g., Onoue et al. 2019; Yang et al. 2021; Farina et al. 2022; Mazzucchelli et al. 2023) and thus provide stringent constraints on the formation and evolution of the very first massive black holes (Inayoshi et al. 2020; Fan et al. 2023). Only a handful of quasars beyond $z > 7$ have been identified to date (Mortlock et al. 2011; Bañados et al. 2018; Yang et al. 2020; Wang et al. 2021). The scarcity of confirmed sources at the quasar redshift frontier is generally attributed to two main factors: (1) the intrinsic steep decline in the space density of luminous quasars with increasing redshift, as captured by the quasar luminosity function at $z > 6$ (e.g., Schindler et al. 2023; Matsuoka et al. 2023); and (2) the fact that quasars at $z \sim 7.1 - 7.5$ exhibit optical/NIR colours that are nearly indistinguishable from those of Galactic L- and T-dwarfs (e.g., Hewett et al. 2006; Lodieu et al. 2007; Mortlock et al. 2009; Fan et al. 2023; Bañados et al. 2025a).

The recent discovery of reionization-era blazars (Belladitta et al. 2020; Ighina et al. 2024; Wolf et al. 2024; Bañados et al. 2025b; Marcotulli et al. 2025), however, suggests a third possibility for the rarity of $z > 7$ quasars: many of these objects may be systematically missed in restframe UV searches because they are undergoing obscured growth, enshrouded in dense gas and/or dust (e.g., Maiolino & Rieke 1995; Assef et al. 2015; Vito et al. 2019b; Ni et al. 2020; Lambrides et al. 2020; Gilli et al. 2022). The fraction of obscured quasars has been shown to increase with redshift (e.g., Buchner et al. 2015; Liu et al. 2017; Glikman et al. 2018; Lanzuisi et al. 2017; Vito et al. 2018; Iwasa et al. 2020; Gilli et al. 2022; Peca et al. 2023). Indeed, from the Ly α $\lambda 1216$ absorption profiles of quasars at $z > 7$, Davies et al. (2019) inferred extremely low radiative efficiencies ($\leq 0.1\%$), which may indicate that these quasars remain obscured over nearly the entirety of their growth phases. They constrain the obscured fraction at $z > 7$ to $> 82\%$ at 95% credibility.

This opens an exciting perspective, pointing to the existence of a vast, yet largely unexplored, quasar population at cosmic dawn. Conversely, the few archetypal dust-unobscured, broad-line quasars discovered at $z > 7$ must have already cleared the line of sight to their nuclei and broad-line regions (BLR), perhaps through powerful feedback associated with the so-called “blowout phase” (e.g., Hopkins et al. 2006; Zakamska et al. 2016; Ishibashi et al. 2018; Lansbury et al. 2020; Vayner et al. 2025). Detecting observational signatures of such a recent blowout in the immediate environments of the highest-redshift quasars—for instance, fossil distributions of expelled dense gas or dust—would offer a robust anchor for embedding these extremely rare sources within a broader evolutionary sequence.

The James Webb Space Telescope (JWST, Gardner et al. 2006)/Near-Infrared Camera (NIRCam, Rieke et al. 2023) has ushered in a new era by enabling, for the first time, detection of restframe ultra-violet (UV) and optical emission from the host galaxies of quasars at $z > 6$ (Ding et al. 2022, 2023; Stone et al. 2023; Yue et al. 2024). To overcome the stark contrast between the unresolved, dominant quasar light and the compact,

faint stellar continuum emission at these wavelengths and redshifts, a detailed model of the instrument’s point-spread function (PSF) is essential (e.g., Mechtley et al. 2012). With advanced imaging PSF subtraction techniques, it is now possible to directly measure the host galaxy’s stellar mass from the extended continuum emission detected with JWST, and to compare it with the central SMBH mass to assess whether their growth was offset with respect to local scaling relations (e.g. Magorrian et al. 1998; Ferrarese & Merritt 2000; Gebhardt et al. 2000; Häring & Rix 2004; Kormendy & Ho 2013; Reines & Volonteri 2015; Habouzit et al. 2021). The JWST Near-Infrared Spectrograph Integral Field Unit (NIRSpec IFU, Böker et al. 2022) enables integral field spectroscopy over tens of kiloparsecs around high-redshift quasars and AGN, providing simultaneous access to the host galaxy’s stellar continuum, the quasar spectrum (e.g. Loiacono et al. 2024), and gas kinematics in the quasar vicinity—revealing quasar feedback (e.g. Liu et al. 2024) and large-scale interactions with companion galaxies (e.g., Marshall et al. 2023, 2024; Decarli et al. 2024; Übler et al. 2024). Similarly to NIRCam, detailed PSF modelling techniques are required to disentangle the quasar from underlying gas emission (e.g., Wylezalek et al. 2022; Veilleux et al. 2023; Perna et al. 2023; Vayner et al. 2024; Marshall et al. 2023, 2024).

At $z_{\text{[CII]}} = 7.6423$, the quasar J031343.84–180636.4 (hereafter J0313–1806) is currently the most distant system known in which the properties of a matured $> 10^8 M_\odot$ SMBH, its host and direct environment can be studied in detail (Wang et al. 2021). The virial single-epoch estimate of the SMBH mass, M_{BH} , based on the broad Mg II $\lambda 2800$ emission line is $(1.6 \pm 0.4) \times 10^9 M_\odot$ and Atacama Large Millimeter Array (ALMA) observations indicate a high cold dust mass of $\sim 7 \times 10^7 M_\odot$. From its [CII] $\lambda 157.6 \mu\text{m}$ emission, Wang et al. (2021) further derive a high star-formation rate $\text{SFR}_{\text{[CII]}} = 40\text{--}240 M_\odot \text{ yr}^{-1}$. In its restframe UV spectrum, the object shows signatures of strong outflows through broad absorption lines in CIV $\lambda 1549$, S IV $\lambda\lambda 1394, 1403$ and tentatively in Mg II $\lambda 2800$ (up to $0.19c$), as well as a significant blueshift of its CIV $\lambda 1549$ broad emission line ($\sim 3100 \text{ km s}^{-1}$). The immediate environment of this quasar is therefore expected to show complex kinematics.

We present a study aimed at resolving the kinematic structure of the extended, restframe optical ionized gas emission within ~ 15 kpc of J0313–1806 in both spectral and spatial dimensions with the JWST/NIRSpec Integral Field Unit (IFU, Cycle 1 GO 1764). In Section 2, we describe the JWST/NIRSpec IFU observations of J0313–1806 and the associated data reduction. Section 3 focuses on the nuclear quasar spectrum, from which we derive the central SMBH properties. In Section 4, we detail our PSF subtraction procedure and recover the extended gas emission in the quasar’s immediate environment. Finally, in Section 5, we synthesize the results from the nuclear spectrum and the extended emission to place them in a broader physical context. We present our conclusions in Section 6.

Throughout this paper, we assume a concordance ΛCDM cosmology with parameters: $H_0 = 70 \text{ km s}^{-1}$, $\Omega_M = 0.3$, $\Omega_\Lambda = 0.7$. With this cosmology, one second of arc corresponds to 4.96 kpc in proper (physical) transverse distance at $z = 7.64$. All equivalent widths are restframe measurements. All images are shown in the north-up, east-left convention.

2. Observations and data reduction

2.1. JWST/NIRSpec IFU pointings

We observed J0313–1806 and an associated PSF calibration star, TYC 5875-488-1, with JWST/NIRSpec IFU on Jan 21, 2023, as part of our JWST Cycle 1 proposal ID 1764. The total exposure times were 9.82 and 0.17 hours, respectively. The grating and filter combination G395M/F290LP covers wavelength range 2.87–5.10 μm with a nominal resolving power of $R \sim 1000$. The velocity resolution of our cube is thus roughly 300 km s^{-1} . The field of view of JWST/NIRSpec IFU is $3'' \times 3''$ (corresponding to $\sim 15 \text{ kpc} \times 15 \text{ kpc}$ at the redshift of the quasar), with a native pixel scale of $0.1''$. The NIRSpec IFU PSF is undersampled by design. A small cyclic 8-point dithering pattern was chosen to improve spatial sampling. This observing strategy alleviates aliasing effects arising from the undersampled PSF (so-called *wiggles*, e.g. Perna et al. 2023). Each dither consists of 3 integrations of 20 groups each. The readout pattern was set to NRSIRS2. In addition to the cyclic dithers, an additional *leakcal* exposure was taken to monitor and correct for light leaks from the neighbouring micro-shutter-array (MSA) on JWST.

2.2. Data reduction

We reduced the data cubes with the standard three-stage JWST Science Calibration Pipeline¹ version 1.15.0 (CRDS context: `jwst_1322.pmap`). The first stage, `calwebb_detector1`, performs group-level corrections on uncalibrated data such as detector bias and dark subtractions, electronic noise, persistence and linearity corrections. It also detects cosmic rays (`jump`), converts counts to electrons, and fits a slope to the counts to calculate fluxes (`ramp_fitting`). We inserted the additional processing step `nsclean` between the cosmic-ray `jump` detection and `ramp_fitting` steps², which removes all correlated read noise from the frames. The output of the first calibration stage is a set of so-called rate images that form the input to the second stage `calwebb_spec2`, which encompasses 2D spectroscopic processing steps such as flat-fielding, slitlet extraction, background subtraction, as well as wavelength and flux calibrations. The output of this stage is a set of 2D spectral images for each slitlet. The final stage, `calwebb_spec3`, combines the individual spectra into a cube, ensuring astrometric coherence. An outlier rejection step removes residual artefacts by searching for pixels that display a sharp difference with respect to their neighbours in the spatial direction. The calibration stage includes three cube projection algorithms: 3D drizzle, weighting, and the estimated median signal method. We opted for 3D drizzle, which projects pixel flux from different dithers onto a common 3D grid, accounting for the relative pixel-to-pixel and pixel-to-voxel overlap. The major advantage of 3D drizzle is that it is particularly adapted to undersampled data by accessing sub-pixel scales, leveraging the input from multiple dithers. The cyclic dithering pattern allows us to reproject our data cube to a half-pixel scale of $0''.05$ ³, thus improving spatial sampling. At the redshift of the quasar, $z = 7.6423$, this corresponds to a projected physical scale of $\sim 0.2 \text{ kpc/pixel}$. However, the code assumes a rigid one-to-one mapping of the illuminated chip x- and y-axis and the dispersion and spatial dimensions of the instrument. This in-

troduces undersampling artefacts that were addressed in the additional pre-processing step detailed in Appendix A.

The red continuum imprinted by the zodiacal and stray light background was accounted for by sigma-clipping the reduced cubes in flux, masking three sigma outliers. The unmasked regions are treated as field spaxels. We extract the median 1D continuum from these spaxels and subtracted it from the cubes.

3. Physical properties of the black hole

3.1. Spectral fitting

To determine the properties of the SMBH powering J0313–1806, we apply the same methodology as Liu et al. (2024). We extracted the quasar spectrum by identifying the spaxel with the highest integrated flux, which was defined as the location of the unresolved quasar emission (pixel (49,46), 0-indexed) within an aperture of radius $0''.35$.

Following Loiacono et al. (2024), we determined the optimal extraction radius for the quasar spectrum by testing values that minimize background and extended emission contamination. Spectra of the PSF star TYC 5875-488-1 were extracted at radii from 3 to 14 pixels ($0''.15$ to $0''.70$) in $0''.05$ steps. We calculate the wavelength-dependent encircled-flux fraction by dividing these extracted spectra by the spectrum extracted in a large reference aperture of $1''.0$ (20 pixels). For each radius, the chromatic flux loss (CFL) was defined as

$$\text{CFL}(R, \lambda) = \frac{f_{\text{blue}} - f_{\text{red}}}{f_{\text{blue}}} \times 100\%,$$

where f_{blue} and f_{red} are the median enclosed-flux fractions measured in the blue ($2.9\text{--}3.5 \mu\text{m}$) and red ($4.5\text{--}5.1 \mu\text{m}$) bands, respectively. Wavelength-dependent flux fractions for all aperture radii are shown in Appendix B. We adopt an extraction radius of $0''.35$ (see also Marshall et al. 2023), which captures the majority of the PSF flux while keeping the chromatic flux loss below the percent level and simultaneously limiting background and extended emission contamination. We note that this radius corresponds to $\sim 1.4 \text{ kpc}$ at the redshift of the quasar and thus completely encompasses the BLR and the classical narrow-line region (NLR, e.g. Baskin & Laor 2005). We model the wavelength-dependent correction by fitting a smooth spline to the $0''.35$ encircled fraction array and apply the correction to the quasar spectrum.

The resulting spectrum is presented in Fig. 1. Notably, the spectrum reveals relatively weak [O III] $\lambda\lambda 4959, 5007$ emission lines and a strong Fe II pseudo-continuum, features that are also observed in the $z = 7.5$ quasar J100758.26+211529.2 (Liu et al. 2024). These characteristics are typical of rapidly accreting quasars (see discussion in Sec. 5).

To analyze the spectrum, we used the public software PyQSOFit (Guo et al. 2018; Shen et al. 2019; Ren et al. 2024). We selected featureless spectral regions ($4000 - 4200 \text{\AA}$, $4500 - 4700 \text{\AA}$, and $5050 - 5750 \text{\AA}$), to fit the quasar continuum. Our setup uses a power-law, a restframe optical Fe II template (Park et al. 2022) covering the H β $\lambda 4861$ (H β) region and an additional smooth second-order polynomial correction term to adjust the tilt and curvature of the fit. We fixed the redshift of the quasar at $z = 7.6423$ (as measured from [C II] $\lambda 157.6 \mu\text{m}$ by Wang et al. 2021). After subtracting the best-fit pseudo-continuum, we fitted the H β emission line with three broad Gaussians ($\text{FWHM} > 1200 \text{ km s}^{-1}$), as well as one narrow Gaussian ($\text{FWHM} < 1200 \text{ km s}^{-1}$). The

¹ <https://jwst-docs.stsci.edu/jwst-science-calibration-pipeline>

² <https://science.nasa.gov/mission/webb/for-scientists/#NSClean>

³ <https://jwst-docs.stsci.edu/jwst-near-infrared-spectrograph/nirspec-observing-strategies/nirspec-dithering-recommended-strategies#gsc.tab=0>

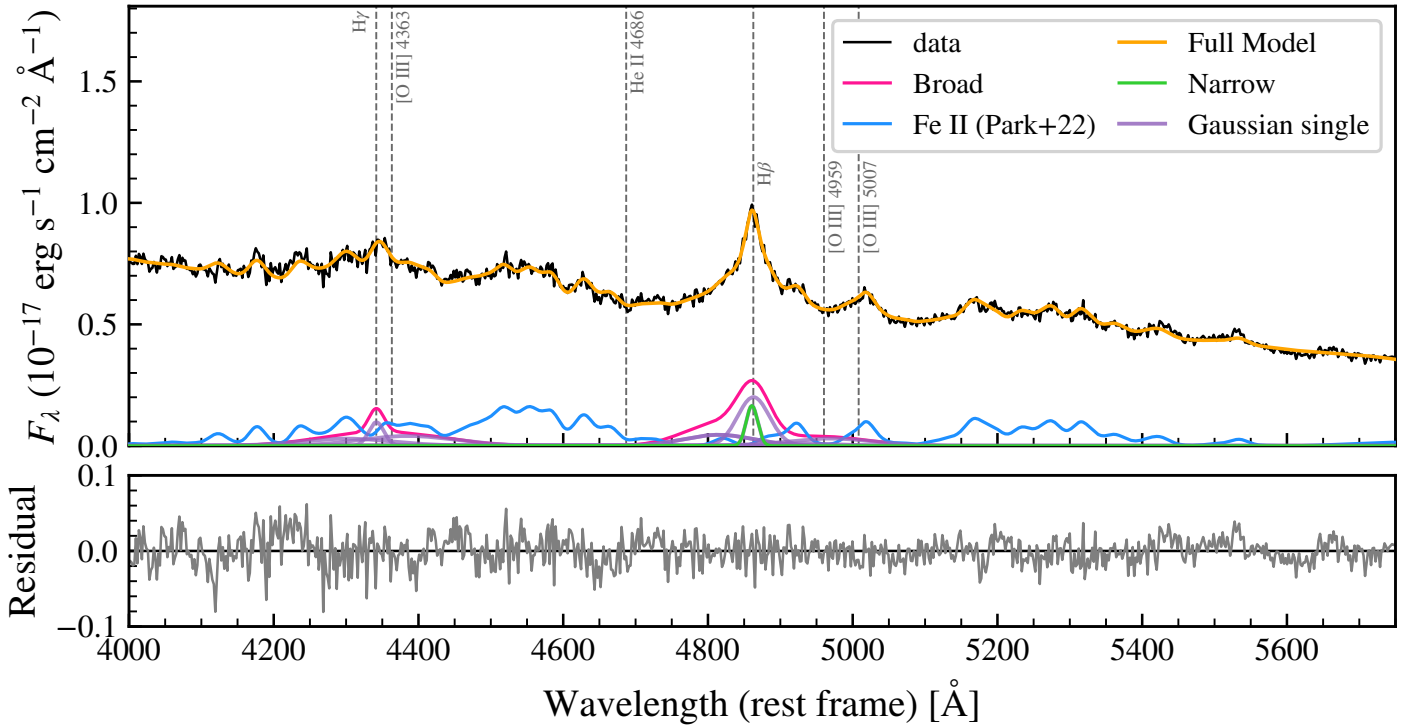


Fig. 1. Extracted quasar spectrum within a 0.35 aperture centred on the spaxel with the highest integrated flux. The observed spectrum, shown in black, is well fit by the PyQSOFit model, shown in orange. Broad $H\beta$ and $H\gamma$ are modelled using three and two broad Gaussian components (pink lines, individual Gaussians are shown in purple) with $\text{FWHM} > 1200 \text{ km/s}$, and one Gaussian component with $\text{FWHM} < 1200 \text{ km/s}$ to trace narrow components (green line). The $[\text{O III}] \lambda\lambda 4959, 5007$ emission lines are modelled with one broad and one narrow component. No narrow $[\text{O III}] \lambda\lambda 4959, 5007$ components are detected, while a strong contribution from Fe II emission (blue line) is evident (Park et al. 2022). The lower panel shows fit residuals.

Akaike (AIC) and Bayesian (BIC) information criteria both indicate that a three-component broad $H\beta$ model is ideal. Adding additional components does not significantly improve the χ^2 , while a two-component model underfits the line profile. We fit $H\gamma \lambda 4340$ ($H\gamma$) with two broad and one narrow component. The $[\text{O III}] \lambda 4959$ and $[\text{O III}] \lambda 5007$ lines are fit with one broad and one narrow Gaussian each. In all fits, the flux ratios of the $[\text{O III}] \lambda\lambda 4959, 5007$ doublet were constrained to their theoretical values, $F_{5007}/F_{4959} = 2.98$ (e.g., Storey & Zeippen 2000). In our fit, the narrow core of the $[\text{O III}] \lambda\lambda 4959, 5007$ lines collapsed to zero flux. Very weak wings of the $[\text{O III}] \lambda\lambda 4959, 5007$ lines are detected ($\text{EW}([\text{O III}] \lambda 5007) \approx 0.02 \text{ \AA}$), however this is sensitive to the continuum placement and to the adopted decomposition of the $H\beta$ base. We thus treat the $[\text{O III}] \lambda\lambda 4959, 5007$ as not significantly detected and quote a 3σ upper limit on the equivalent width of $[\text{O III}] \lambda 5007$ measured from the local continuum noise, assuming a Gaussian line profile with a fixed FWHM of 19 \AA : $\text{EW}([\text{O III}] \lambda 5007) < 1.42 \text{ \AA}$ (based on the width of the detected narrow $H\beta$ component). The broad-line Balmer decrement shows no evidence for BLR reddening. The resulting best-fit spectrum, along with the fits for the broad emission lines and the Fe II model components, is presented in Fig. 1.

3.2. Black hole mass and Eddington rate

Our best-fit broad Gaussian $H\beta$ model (i.e. excluding the narrow component) has an FWHM of $4156 \pm 68 \text{ km s}^{-1}$, which we interpret as virial broadening in the BLR (e.g., Peterson 2006). The instrumental broadening of the NIRSpec G395M/F290LP configuration is negligible compared to the measured broad $H\beta$ width. Its error is dominated by the statistical uncertainty; we

therefore do not apply an instrumental broadening correction. We measured the best-fit continuum monochromatic luminosity at restframe 5100 \AA . To account for systematics, we added a conservative 10% flux calibration uncertainty in quadrature to the small statistical error⁴, obtaining $L_{5100} = (1.77 \pm 0.18) \times 10^{46} \text{ erg s}^{-1}$. Together with the measured $H\beta$ line width, this allows us to estimate the black hole mass M_{BH} of the central SMBH using single-epoch calibrations, such as Greene & Ho (e.g., 2005); Vestergaard & Peterson (e.g., 2006); Shen et al. (e.g., 2024), following Kaspi et al. (2000). We use the parametrisation of Shen et al. (2024):

$$\log\left(\frac{M_{\text{BH}}}{M_{\odot}}\right) = 0.85 + 0.50 \log\left(\frac{L_{5100}}{10^{44} \text{ erg s}^{-1}}\right) + 2.0 \log\left(\frac{\text{FWHM}_{H\beta}}{\text{km s}^{-1}}\right), \quad (1)$$

with an intrinsic scatter of $\sigma_{\text{int}} = 0.45 \pm 0.04 \text{ dex}$.

We obtain an $H\beta$ single-epoch mass of $M_{\text{BH}, H\beta} = (1.63 \pm 0.10) \times 10^9 M_{\odot}$, and $M_{\text{BH}, H\beta} = (1.63^{+2.97}_{-1.05}) \times 10^9 M_{\odot}$ when accounting for the intrinsic scatter. We use the measurements of Mg II $\lambda 2800$ and L_{3000} reported by Wang et al. (2021) to revisit the black hole mass estimate using the Mg II $\lambda 2800$ single-epoch calibration of Shen et al. (2024), yielding $M_{\text{BH}, \text{Mg II}} = (3.18 \pm 1.06) \times 10^9 M_{\odot}$, or $M_{\text{BH}, \text{Mg II}} = (3.18^{+6.26}_{-2.11}) \times 10^9 M_{\odot}$ when including intrinsic scatter. Considering measurement uncertainties alone, the two estimates differ at the $\sim 1.8\sigma$ level. When the intrinsic scatter of the calibrations is included, the results are fully consistent. We note that using the Shen et al. (2024) calibration for the Mg II $\lambda 2800$ -based black hole mass yields values that

⁴ We apply this 10% uncertainty floor to all subsequent flux and equivalent width measurements.

Quantity	Units	Value
FWHM _{Hβ} ⁽¹⁾	km s ⁻¹	4156 ± 68
$L_{5100}^{(2)}$	erg s ⁻¹	(1.77 ± 0.18) × 10 ⁴⁶
EW(H β) ⁽³⁾	Å	53.18 ± 0.31
EW([OIII]) ⁽⁴⁾	Å	< 1.42
EW(FeII) ⁽⁵⁾	Å	38.46 ± 0.02
F([OIII]) ⁽⁶⁾	erg s ⁻¹ cm ⁻²	< 2.39 × 10 ⁻¹⁸
$M_{\text{BH},\text{H}\beta}^{(7)}$	M_{\odot}	(1.63 ± 0.10) × 10 ⁹
$L_{\text{bol}}^{(8)}$	erg s ⁻¹	(1.64 ± 0.16) × 10 ⁴⁷
$L_{\text{bol}}/L_{\text{Edd}}^{(9)}$	–	0.80 ± 0.05

Table 1. Results of spectral fitting for J0313–1806. (1) Full-width-at-half-maximum of the broad H β line (2) Monochromatic luminosity at 5100 Å (3) Equivalent width of the broad H β line (4) 3 σ upper limit on the equivalent width of [O III] λ 5007 (5) Equivalent width of the Fe II blend at 4434–4684 Å (6) 3 σ upper limit on the flux of [O III] λ 5007 (7) Black hole mass derived based on Shen et al. (2024) (8) Bolometric luminosity based on Richards et al. (2006) (9) Eddington rate

are higher by a factor of ∼ 2 compared to those obtained with the Vestergaard & Osmer (2009) calibration adopted by Wang et al. (2021) and Yang et al. (2021); the two estimates are consistent only when accounting for the intrinsic scatter of the relations.

We calculate the Eddington rate λ_{Edd} , defined as the ratio of bolometric luminosity L_{bol} and the Eddington luminosity $L_{\text{Edd}} = \frac{4\pi GM_{\text{BH}}m_pc}{\sigma_T}$, where m_p is the proton mass, c is the speed of light, and σ_T is the Thomson scattering cross-section. We derive the bolometric luminosity using the bolometric correction factor from Richards et al. (2006), applying $L_{\text{bol}} = 9.26 \times L_{5100}$, which yields $(1.64 \pm 0.16) \times 10^{47}$ erg s⁻¹. From our derived M_{BH} estimate we calculate an Eddington ratio of $\lambda_{\text{Edd}} = 0.80 \pm 0.05$ accounting only for measurement uncertainties. These findings corroborate the results of Wang et al. (2021), indicating that quasar J0313–1806 harbours a relatively mature SMBH accreting at a high Eddington rate. The results of the spectral fit are summarized in Table 1.

4. Extended nebular emission

4.1. Point-spread-function modelling

To identify any potential extended gas components linked to the host galaxy, outflows, or field sources in the cube, we must first model and subtract the unresolved light from the significantly more luminous central quasar. Here, we create an empirical model of the PSF based on the observations of the associated PSF star, TYC 5875-488-1. To precisely align the quasar and PSF star images, we first compute the two-dimensional cross-correlation between the quasar and PSF star white-light images obtained by integrating the cubes over the wavelength range 3.5–5.1 μm . This cross-correlation evaluates the similarity between the images at different pixel offsets.

We apply a PSF alignment shift between the brightest spaxels of the collapsed cubes, determining a sub-pixel shift in Fourier space (e.g., Stone et al. 2001; Foroosh et al. 2002). This technique involves computing the Fourier transform of each wavelength slice, applying the calculated phase shift for sub-pixel precision, and then performing an inverse Fourier transform on the shifted data. We obtain x-shift = 1.48 pixels and y-shift = -2.34 pixels. The aligned PSF star cube is computed as:

$$\tilde{I}_{\text{PSF}}(x, y) = \mathcal{F}^{-1} \{ \mathcal{F}[I_{\text{PSF}}(x, y)] \cdot e^{-2\pi i(x_{\text{shift}}, y_{\text{shift}})} \}. \quad (2)$$

To account for the spectral energy distribution (SED) differences between the quasar and the PSF star, we extract integrated spectra using a circular aperture (radius = 7 pixels, i.e. 0''.35). The aperture scale is determined based on the analysis shown in Appendix B. At the chosen radius, the enclosed flux fraction is already within ∼1–2% of that measured with larger apertures, and its wavelength dependence is smooth and consistent with the expected chromatic broadening of the JWST PSF. This indicates that the extracted flux is dominated by unresolved quasar light, with no evidence for a significant contribution from extended host emission.

The raw scaling factor per wavelength is given by $S(\lambda) = F_{\text{quasar}}(\lambda)/F_{\text{PSF}}(\lambda)$. However, small-scale fluctuations in $S(\lambda)$ can introduce systematic artifacts in the residual spectrum. To mitigate this, we apply a Gaussian smoothing filter with $\sigma = 5$ pix along the spectral axis. The spectra and the smoothed wavelength-dependent scale factor are shown in the left panel of Fig. 2. The figure in the right panel shows that the PSF model, i.e. the smoothed and scaled PSF star, accurately traces the flux profile of the quasar.

Once the smoothed scale factors are computed, we apply them to each wavelength slice of the PSF star cube, scaling it to match the quasar SED:

$$I_{\text{PSF, scaled}}(x, y, \lambda) = S_{\text{smooth}}(\lambda) \times \tilde{I}_{\text{PSF}}(x, y, \lambda), \quad (3)$$

where $S_{\text{smooth}}(\lambda)$ denotes the smoothed wavelength-dependent scale factor, and $\tilde{I}_{\text{PSF}}(x, y, \lambda)$ is the subpixel-aligned PSF cube.

The final PSF-subtracted quasar cube is then obtained by subtracting the scaled PSF cube from the observed quasar data:

$$I_{\text{residual}}(x, y, \lambda) = I_{\text{quasar}}(x, y, \lambda) - I_{\text{PSF, scaled}}(x, y, \lambda). \quad (4)$$

The resulting residual cube $I_{\text{residual}}(x, y, \lambda)$ reveals the underlying spatially extended emission that is not associated with the unresolved quasar core. This emission can originate from narrow-line regions, the host galaxy, outflows, satellite companions or chance-aligned field fore- or background sources. A visual overview of the PSF subtraction process is presented in Fig. 3.

Despite the careful modelling and subtraction procedure, several sources of systematic uncertainty remain. First, the SEDs of the quasar and the PSF star differ intrinsically, introducing wavelength-dependent mismatches that are not fully corrected by the smooth scaling procedure. Second, subpixel alignment errors, particularly in the presence of asymmetric PSF wings or optical distortions, can leave residual artifacts in the final cube. We have assessed the impact of these effects through a series of robustness tests. Varying the degree of spectral smoothing applied to the scaling factor $S(\lambda)$ results in negligible changes to the residual maps and does not affect the detection of extended emission. In addition, perturbing the relative alignment between the quasar and PSF star cubes at the level of the measured alignment uncertainty produces only minor changes in the residual root-mean-square (RMS). Residual artifacts associated with these systematics are confined to the central PSF core and do not generate spatially extended or spectrally coherent features. We therefore conclude that these systematic uncertainties do not affect the results or interpretations presented below.

In the collapsed PSF-subtracted cube, we identify three regions of interest. A luminous core close to the quasar position

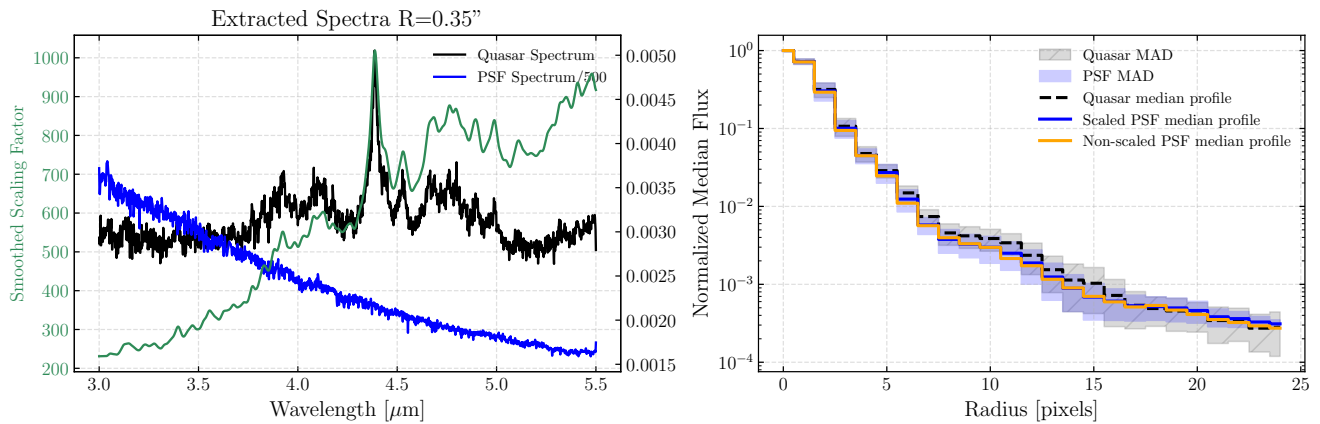


Fig. 2. PSF model. *Left:* Spectral comparison between the quasar and PSF star used to derive the PSF scaling factor. The extracted 1D spectra from the quasar (black) and PSF star (blue) were obtained using a circular aperture with radius $0''.35$. The PSF spectrum is scaled down by a factor of 500 for visual comparison. While the PSF star shows a smooth stellar continuum, the quasar exhibits a prominent broad $H\beta$ emission line and strong $Fe\text{II}$ features. The wavelength-dependent scaling factor $S(\lambda)$ computed as the ratio between the quasar and PSF spectra is shown in green. The scaling factor is smoothed with a Gaussian kernel of width $\sigma = 5$ pix before being applied slice by slice to the aligned PSF cube. *Right:* Median radial profiles extracted from the quasar cube (black dashed), the raw PSF star cube (orange) and the PSF star cube, corrected with the wavelength-dependent scaling factor (blue). The radial profiles are measured from the brightest pixel in white light of each cube. The colour-shaded areas correspond to the median absolute deviations of the quasar radial profile (grey) and the scaled PSF star cube (blue).

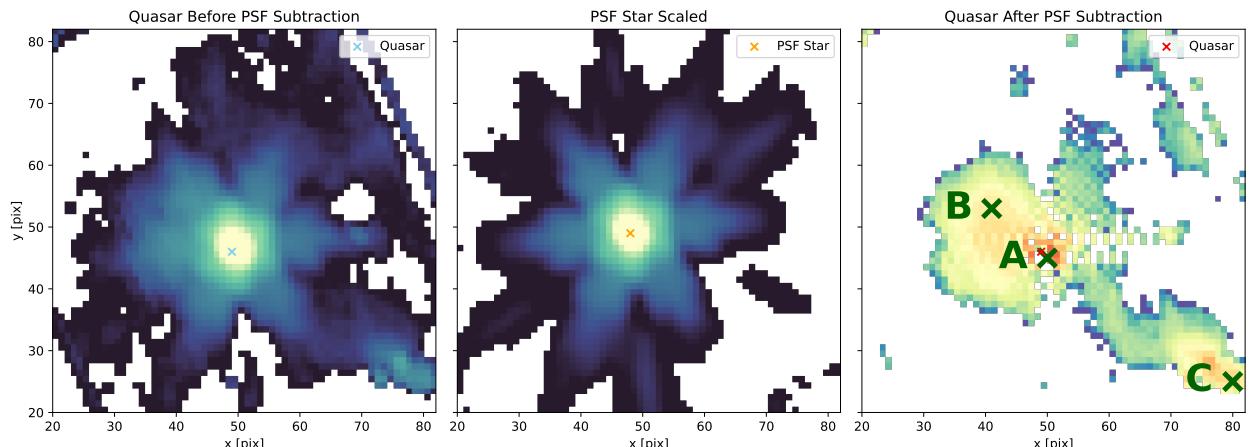


Fig. 3. PSF subtraction procedure for J0313–1806. *Left:* Integrated white-light image of the reduced cube centered on J0313–1806. The blue cross marks the position of the unresolved quasar. *Centre:* Integrated and scaled cube of the PSF calibration star TYC 5875-488-1, aligned and scaled to match the quasar emission. The orange cross marks the position of the unresolved star. *Right:* Residual white-light image of J0313–1806 after PSF subtraction, revealing extended emission components after removal of the unresolved quasar core. We highlight three regions of interest: A) A bright core near the quasar, B) a near-elliptical diffuse region just north-east of the quasar and C) a distinct foreground elliptical source to the south-west of the quasar. This work focuses on the central region A). For all maps, pixels with negative integrated flux were masked.

at pixel (50,45) (see green cross close to A); the object of the present paper. We further identify an extended quasi-elliptical, nebulous region to the north-east (B) of the quasar. The origin of this emission is further discussed in Appendix C. We also find a distinct source to the south-west (C) is spatially co-incident with a foreground galaxy detected in JWST/Near Infrared Camera (NIRCam) and JWST/Mid-Infrared Instrument (MIRI) imaging from the same Cycle 1 programme (#1764). The extracted source has photometry consistent with that of a galaxy at $z \sim 2.25$ (Pudoka et al. 2025, and private communication). A clear detection in the F090W filter consolidates the lower redshift nature of this source. A spectrum extracted at this location displays a strong emission line, fixing the galaxy to $z = 2.30$, through its $Pa\beta \lambda 12818$ line. In Appendix D, we present spectra extracted within $0''.35$ of the emission regions A, B and C. The alternating horizontal pattern near region A is a PSF subtraction artifact

caused by residual structured PSF wings (including diffraction features) and IFU sampling.

4.2. Balmer kinematic moment maps

After PSF subtraction, we fitted the data cube with a combination of host continuum and emission line models using the cube analysis software package q3dfit⁵ (Rupke 2014; Rupke et al. 2021), operating in *fitpoly* mode. We apply Gaussian smoothing with a 2.5 pixel (~ 0.5 kpc) kernel along the spatial dimensions to suppress pixel-to-pixel noise fluctuations and enhance the detectability of low-surface-brightness emission, while also mitigating aliasing effects. The continuum was modeled with a third-order polynomial, while emission lines were fitted with single Gaussian components. Initially, we restricted the line fit-

⁵ <https://github.com/Q3D/q3dfit>

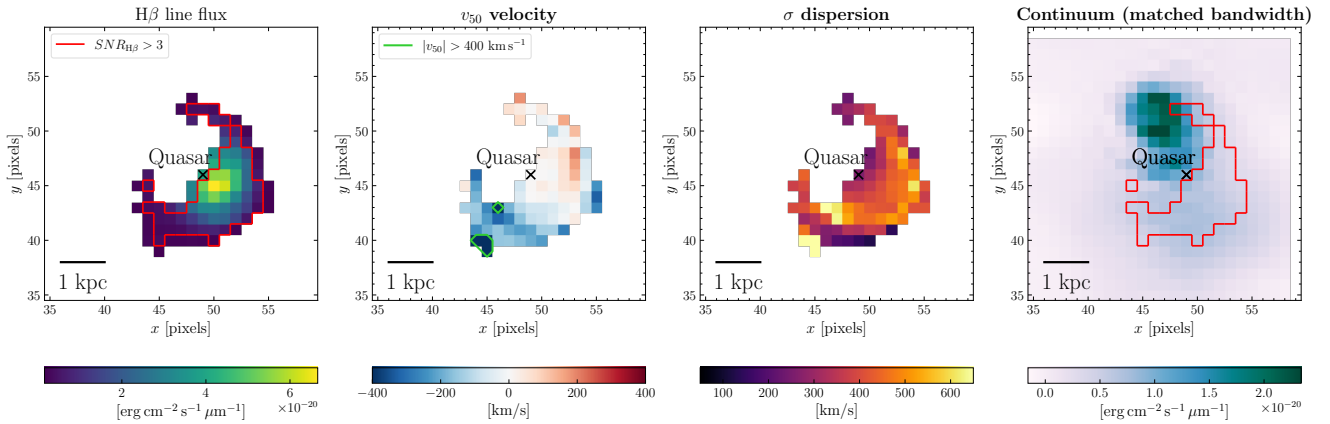


Fig. 4. Kinematic moment maps of $\text{H}\beta$ around J0313-1806 and bandwidth-matched continuum. Gaussian spatial smoothing over 2.5 pixel kernel was applied (at $0''.05/\text{pix}$ scale). *First panel:* Flux map of 3σ detected $\text{H}\beta$ (57 spaxels). These are highlighted by the red contour. We define this distribution as $\text{H}\beta$ shell. Adjunct spaxels in 8-connectivity to these detection spaxels with at least $\text{S/N}_{\text{H}\beta} > 1.5$ are also shown. The flux in the line peaks close to the quasar location, consistent with a central ionizing source. *Second panel:* Velocity offset map as traced by the v_{50} parameter. A clear velocity gradient is observed along the shell, indicating expansion or rotation of the structure. Spaxels with extreme velocities ($|v_{50}| > 400 \text{ km s}^{-1}$) are marked with green contours. *Third panel:* Velocity dispersion, σ . Patches of large dispersions ($>600 \text{ km/s}$) are observed at the edges and to the south-east of the structure, potentially indicating highly turbulent gas motion. *Fourth panel:* Continuum map constructed by integrating the fitted continuum model over a line-free spectral window with bandwidth matched to that of $\text{H}\beta$. While elevated continuum emission overlaps spatially with the $\text{H}\beta$ shell, the absence of brightened nuclear morphology in the map following the $\text{H}\beta$ flux confirms that the observed $\text{H}\beta$ structure is not driven by background variations or continuum residuals. The continuum map shows a clear flux peak offset to the north from the quasar position. This component does not trace the shell-like $\text{H}\beta$ morphology and lacks any associated kinematic structure. We therefore interpret it as artifact from imperfect fitting in imperfectly PSF-subtracted spaxels, rather than extended stellar or nebular continuum emission.

ting to $[\text{O III}]\lambda 5007$ and the Balmer lines $\text{H}\beta$ and $\text{H}\gamma$, with the Balmer lines kinematically tied. We stress that $[\text{O III}]\lambda 5007$ and the Balmer lines are fitted individually, allowing the code to trace kinematically distinct regions. Prior to fitting, the model spectra were convolved to match the spectral resolution of the G395M grating. We allow the code to fit lines up to $\sigma = 2,500 \text{ km s}^{-1}$ (FWHM $\approx 5,900 \text{ km/s}$), a permissive upper bound for extended ionized gas around a quasar. We obtain zeroth, first and second order kinematic moments using `q3dfit`. The flux map are obtained from the single-Gaussian line fits. No spaxel with $[\text{O III}]\lambda\lambda 4959,5007$ ($\text{S/N} > 3$ in flux) is detected. While we cannot exclude that this is an artifact of the PSF subtraction procedure, we treat $[\text{O III}]\lambda\lambda 4959,5007$ as non-detected. For $\text{H}\beta$ we apply a signal-to-noise threshold $\text{S/N}_{\text{H}\beta} > 3$ on the 0-th moment maps. Adjunct spaxels in 8-connectivity to these detected spaxels with at least $\text{S/N}_{\text{H}\beta} > 1.5$ are also conserved for plotting purposes only. The moment maps are displayed in Fig. 4. Pixels not fulfilling this criterion are masked. The $\text{H}\beta$ emission region forms an envelope or shell-like structure centred on the quasar. 57 spaxels have robustly detected $\text{H}\beta$ with $\text{S/N}_{\text{H}\beta} > 3$ and extend over a region of radius of $\sim 1.79 \text{ kpc}$ of the quasar position. We formally refer to this structure as the $\text{H}\beta$ shell. We further identify 46 spaxels with $1.5 < \text{S/N}_{\text{H}\beta} < 3$, which are in 8-connectivity to neighboring spaxels in which $\text{H}\beta$ is 3σ detected. While kinematically tied to $\text{H}\beta$, $\text{H}\gamma$ is only detected in 11/57 of the $\text{S/N}_{\text{H}\beta} > 3$ spaxels at an integrated $\text{S/N}_{\text{H}\gamma} > 2$. The average projected distance of these spaxels to the quasar is 1.06 kpc. The velocity offset is traced by the v_{50} parameter, i.e., the shift in velocity space at 50% of the line intensity. We note that the detection of parts of the $\text{H}\beta$ shell is also warranted with less aggressive spatial smoothing, e.g. a kernel of 1 pixel.

We first observe that the total fitted line flux map of $\text{H}\beta$ shows an arc-like shape with a flux maximum in the center of the shell at the pixel (50,45), near the unresolved quasar position (49,46), supporting the presence of a central ionizing source, i.e.

the actual AGN or a nuclear central star cluster. The slight offset between the $\text{H}\beta$ -flux peak and the quasar position is within the FWHM of the JWST PSF and is attributable to residual PSF subtraction effects. In Fig. 4, the v_{50} map displays a clear velocity dipole from blueshifts to redshifts south-east to north-west. We measure a median blueshifted ($v_{50} < 0 \text{ km s}^{-1}$) velocity $v_{50,\text{blue}} = -113_{-27}^{+17} \text{ km s}^{-1}$ and a median redshifted ($v_{50} > 0 \text{ km s}^{-1}$) velocity $v_{50,\text{red}} = 32_{-8}^{+4} \text{ km s}^{-1}$. The gradient of the velocity field appears centred on the quasar. The offset values are typical of AGN outflows (e.g., Liu et al. 2024). The symmetric, ordered nature of the velocity field around the quasar indicates a coherent large-scale kinematic pattern, consistent with a tilted or partial expanding shell of ionized gas (e.g., Ishibashi et al. 2021), although other complex organized motions (e.g. rotation Ishikawa et al. 2025 or a biconical flow) cannot be excluded. The apparent arc-like geometry of the nebula might also be due to PSF-over-subtraction close to the quasar, effectively depleting signal in $\text{H}\beta$. For simplicity we will assume a spherical shell-like geometry (i.e. a complete sphere around the quasar) while acknowledging that this might not fully capture the real structure of the ionized gas. Finally, the dispersion map shows strong velocity dispersions, with a median dispersion of $\sigma = (415 \pm 51) \text{ km s}^{-1}$. Such dispersions are typically associated with AGN outflows and turbulent gas motion (e.g., Wylezalek et al. 2022). Spaxels corresponding to extreme velocity offsets in the v_{50} map, i.e. $|v_{50}| > 400 \text{ km s}^{-1}$ shown with green contours, appear to also correspond to the highest dispersions $\sigma > 600 \text{ km s}^{-1}$. We note that we cannot fully exclude the possibility, that the observed $\text{H}\beta$ distribution is directly tracing the host galaxy of J0313-1806 or a merging companion. Deep restframe UV/optical imaging with JWST/NIRCam will be required in the future to investigate the presence of a possible co-spatial stellar continuum. In Fig. 4 the control continuum map is constructed by integrating the continuum model over a line-free spectral window with bandwidth matched to that of $\text{H}\beta$ (three times the median velocity σ

of $H\beta$), does not reproduce the peaked structure seen in the line emission, indicating that the observed structure is not driven by continuum or background systematics.

Considering only the 57 spaxels with at least a 3σ detection of $H\beta$, we constructed a mean stacked spectrum of the shell shown Fig. 5. The $H\beta$ line is clearly detected, while $[\text{O III}] \lambda 5007$ remains undetected, and with a median $S/N_{H\gamma} = 1.44$, $H\gamma$ is not detected. We also show the mean stacked spectra, split by their v_{50} values, to highlight differences in the $H\beta$ line profile between blueshifted ($v_{50} < -25 \text{ km s}^{-1}$) and redshifted ($v_{50} > 25 \text{ km s}^{-1}$) regions of the $H\beta$ shell. The blueshifted spaxels exhibit a slightly higher continuum and weaker emission lines compared to the redshifted ones.

We compute the integrated 3σ upper limit on $[\text{O III}] \lambda 5007$ in the $H\beta$ shell (57 spaxels with $H\beta$ at $\text{SNR} > 3$) as

$$F_{[\text{O III}] < 3\sigma} = 3 \sqrt{\sum \sigma_{ij, [\text{O III}]}^2}, \quad (5)$$

where $\sigma_{ij, [\text{O III}]}$ is the per-spaxel 1σ noise uncertainty in the spectrum at the location of $[\text{O III}]$.

The corresponding integrated flux ratio upper limit is then

$$\log_{10} \left(\frac{F([\text{O III}])}{F(H\beta)} \right)_{< 3\sigma} = \log_{10} \left(\frac{F_{[\text{O III}] < 3\sigma}}{\sum_{ij} F_{ij}(H\beta)} \right) = -1.15, \quad (6)$$

where $F_{ij}(H\beta)$ is the spaxel-wise flux measured in the 3σ -detected $H\beta$ line. The integrated flux of $[\text{O III}] \lambda 5007$ in the extended ionized shell is thus lower than $10^{-1.15} \sim 7.1\%$ the integrated $H\beta$ flux at the 3σ confidence level. Using the same methodology we also measure the 3σ upper limit on the $\text{He II } \lambda 1640$ to $H\beta$ ratio in the $H\beta$ nebula. We obtain $\log_{10} \left(\frac{F([\text{He II}])}{F(H\beta)} \right)_{< 3\sigma} = -1.15$.

5. Discussion

We discuss separately the nuclear (Sec. 5.1) and kiloparsec-scale (Sec. 5.2) properties derived for J0313–1806. We discuss our interpretation of the results as evidence for episodic feedback cycles in Sec. 5.3.

5.1. Suppressed nuclear $[\text{O III}]$ emission

The nuclear quasar spectrum displays a broad $H\beta$ line and strong Fe II emission, while $[\text{O III}] \lambda\lambda 4959, 5007$ emission is absent (Fig. 1). Weak or absent $[\text{O III}] \lambda\lambda 4959, 5007$ emission is not uncommon in quasar samples across cosmic time (e.g., Netzer et al. 2004). In the following, we discuss similar objects in the literature and possible physical origins for the lack of $[\text{O III}] \lambda\lambda 4959, 5007$ in J0313–1806.

5.1.1. A high- z weak line quasar?

Weak-line quasars (WLQs) are AGN with absent or very low equivalent-width broad UV emission lines, most prominently the high-ionization lines (e.g. $\text{C IV } \lambda 1549$, $\text{He II } \lambda 1640$). The resonant low-ionization line $\text{Ly}\alpha \lambda 1216$ is often also weak, and mid-ionization lines (e.g. $\text{C III } \lambda 1909$], $\text{Si III } \lambda 1892$]) are frequently damped (Fan et al. 1999; Diamond-Stanic et al. 2009; Shemmer et al. 2010; Plotkin et al. 2015; Chen et al. 2024). The number density of WLQs appears to increase with redshift, with a fraction of roughly 10 – 15% at $z \sim 6$ (Bañados et al. 2016; Shen et al. 2019), compared to 1.3% in the *Sloan Digital Sky Survey* (SDSS; York et al. 2000) at $z \lesssim 4.2$ (Diamond-Stanic et al. 2009).

Broad UV high-ionization line measurements for J0313–1806, in particular $\text{C IV } \lambda 1549$, have already been presented by Yang et al. (2021). They report a $\text{C IV } \lambda 1549$ restframe equivalent width $\text{EW} = 14.2 \pm 0.9 \text{ \AA}$ and a blueshift of $\text{C IV } \lambda 1549$ relative to the systemic redshift from $[\text{C II}] \lambda 157.6 \mu\text{m}$ of $\Delta v_{\text{CIV}-[\text{CII}]} = -4138 \pm 350 \text{ km s}^{-1}$. This makes the line slightly stronger than the canonical $\text{EW} < 10 \text{ \AA}$ criterion used to define WLQs by (Diamond-Stanic et al. 2009, see also Shemmer et al. 2010; Wu et al. 2011; Luo et al. 2015; Plotkin et al. 2015; Chen et al. 2024), but consistent with the $\text{EW} < 15 \text{ \AA}$ criterion adopted by Ni et al. (2018); Timlin et al. (2020). J0313–1806 thus lies at the boundary of commonly adopted WLQ definitions and could be considered a weak-line quasar under the more inclusive criterion.

The combined $\text{C IV } \lambda 1549$ equivalent width and strong blueshift of J0313–1806 are consistent with those of WLQs (see Fig. 2 of Ni et al. 2018 and Fig. 9 of Timlin et al. 2020), and are well offset from the locus of typical quasars. To quantify this behavior in a way that reduces the degeneracy between $\text{C IV } \lambda 1549$ EW and blueshift, we adopt the $\text{CIV} \parallel \text{Distance}$ metric (Rivera et al. 2020, 2022, computed following Ha et al. 2023). This metric combines the two observables into a single scalar quantity that measures how far a source lies along the empirical $\text{C IV } \lambda 1549$ sequence defined by the quasar population, with larger values corresponding to more extreme $\text{C IV } \lambda 1549$ properties. The resulting the $\text{CIV} \parallel \text{Distance}$ for J0313–1806 is ≈ 1.10 . At the independently measured $H\beta$ -based accretion rate of $L_{\text{bol}}/L_{\text{Edd}} = 0.80 \pm 0.05$, this value is consistent with the locus occupied by WLQs in the $\text{C IV} \parallel \text{Distance} - L_{\text{bol}}/L_{\text{Edd}}$ plane (Ha et al. 2023), supporting the classification of J0313–1806 as WLQ-like.

We measured the restframe equivalent widths of $H\beta$ and the Fe II in the 4434 – 4684 \AA spectral window from the quasar spectrum extracted in Section 3.1. The equivalent width of the fitted broad $[\text{O III}] \lambda\lambda 4959, 5007$ wings is extremely small ($\approx 0.02 \text{ \AA}$) and we thus obtained a conservative 3σ upper limit for the equivalent width of $[\text{O III}] \lambda 5007$ in the spectral window 4988 – 5028 \AA . We obtain $\text{EW}(H\beta) = 53.18 \pm 0.31 \text{ \AA}$, $\text{EW}(\text{Fe II}) = 38.46 \pm 0.02 \text{ \AA}$ and $\text{EW}([\text{O III}] \lambda 5007) < 1.42 \text{ \AA}$ (see Table 1) and compare these values to the WLQ sample of Chen et al. (2024), as well as to a control sample of typical SDSS quasars (135,738 quasars with $\text{EW}(H\beta)$ and $\text{EW}([\text{O III}])$ values from data release 16, DR16Q, Lyke et al. 2020; Wu & Shen 2022) in Fig. 6. The $[\text{O III}] \lambda\lambda 4959, 5007$ emission in J0313–1806 is particularly weak relative to its $H\beta$ emission, even when compared to typical WLQs.

The physical driver of the UV-line weakness in WLQs remains debated. One possibility is that the BLR is “anemic,” i.e. has a low gas content and/or covering factor (Shemmer et al. 2010). Alternatively, a soft ionizing continuum could also produce weak high-ionization emission lines. Investigating a sample of seven WLQs, Plotkin et al. (2015) find that their restframe optical low-ionization lines (e.g. $H\beta$) are not as exceptionally weak as their UV lines. These findings favor the soft-ionizing-continuum scenario, since an anemic BLR would result in all broad lines being similarly weak.

Plotkin et al. (2015) further report typical $H\beta$ widths with $\text{FWHM} < 4000 \text{ km s}^{-1}$, strong Fe II emission, and large $\text{C IV } \lambda 1549$ blueshifts (up to 5500 km s^{-1}). As many as $\sim 50\%$ of all WLQs are X-ray weak (e.g., Wu et al. 2011; Luo et al. 2015; Ni et al. 2018, 2022; Pu et al. 2020) relative to typical restframe UV-to-X-ray ratios in Type 1 AGN (Steffen et al. 2006). The hard X-ray spectra of X-ray weak WLQs (typical photon index range,

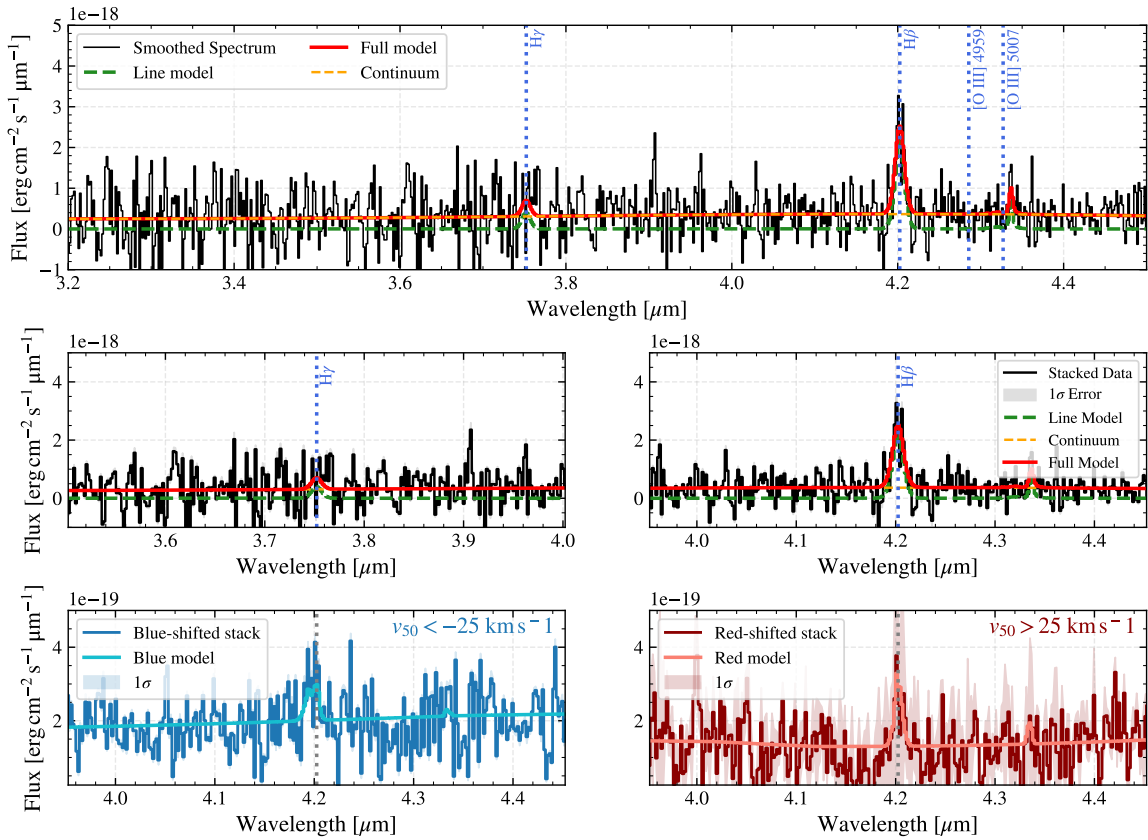


Fig. 5. *Upper panel:* Mean spectrum of the Balmer shell. This spectrum was extracted from 57 spaxels with at least 3σ $\text{H}\beta$ detections. The line (green dashed line), the continuum (orange dashed line), and the full (red line) models are from our q3dfit analysis. The fitted, redshifted $[\text{O III}]\lambda\lambda 4959,5007$ and continuum emissions are consistent with noise. *Middle panel:* Zoom in spectra of the $\text{H}\gamma$ and $\text{H}\beta$ regions. *Lower panels:* Mean spectra of blueshifted ($v_{50} < -25 \text{ km s}^{-1}$, left) and redshifted ($v_{50} > 25 \text{ km s}^{-1}$, right) $\text{H}\beta$ spaxels.

$\Gamma \sim 1.1\text{--}1.2$; Luo et al. 2015; Pu et al. 2020) support the idea that absorption and Compton-thick shielding play an important role for the line emission in WLQs (see also Ni et al. 2022).

In the high- or super-Eddington accretion regime, the accretion disk becomes geometrically thick (Abramowicz et al. 1988, see also Abramowicz 2005 and references therein). Once puffed up, the disk can shield the BLR from hard ionizing radiation, resulting in an overall soft SED (Wang et al. 2014; Madau & Haardt 2024; Lupi et al. 2024b; Madau & Haardt 2024). This shielding can explain both the absence of high-ionization lines in WLQs and their observed X-ray weakness. Additionally, the large $\text{C IV}\lambda 1549$ blueshifts observed in WLQ samples (Luo et al. 2015; Plotkin et al. 2015) are consistent with the presence of powerful line-driven winds expected in high or super-Eddington disks (Castor et al. 1975; Murray et al. 1995). Another recurring feature is the weakness of $[\text{O III}]\lambda\lambda 4959,5007$ emission observed in WLQ samples (Leighly et al. 2007; Shemmer et al. 2010; Wu et al. 2011; Plotkin et al. 2015; Ha et al. 2023; Eilers et al. 2023; Chen et al. 2024). In the puffed-up high- L/L_{Edd} scenario, the shielding of $> 35 \text{ eV}$ photons can also naturally explain the absence of $[\text{O III}]\lambda\lambda 4959,5007$ lines in WLQ spectra. The anti-correlation between the strength of $[\text{O III}]\lambda\lambda 4959,5007$ emission and the accretion rate has long been studied in the Eigen-

vector 1 context (EV1, e.g., Boroson & Green 1992; Sulentic et al. 2000; Marziani et al. 2001; Shen & Ho 2014; Wolf et al. 2020). In addition, the Baldwin effect (Baldwin 1977; Zhang et al. 2013; Stern & Laor 2013; Shen & Ho 2014) describes the general decrease in the equivalent width of emission lines, including $[\text{O III}]\lambda\lambda 4959,5007$, with increasing quasar luminosity. Indeed, weak or absent $[\text{O III}]\lambda\lambda 4959,5007$ emission has also been observed in targeted luminous quasar samples, such as the WISE/SDSS-selected hyper-luminous (WISSH) quasar survey (Vietri et al. 2018), which probes the most extreme end of the quasar luminosity function. Vietri et al. (2018) argue that the relative $[\text{O III}]\lambda\lambda 4959,5007$ weakness observed in $\sim 70\%$ of their sample is mainly driven by orientation effects. The NLR is photoionized within the polar ionization cone. When viewed more face-on, i.e., looking down the cone, the bright continuum outshines the projected NLR emission, resulting in a higher continuum-to-NLR ratio than in more edge-on orientations. In addition to high L/L_{Edd} and orientation effects, obscuration by dust or dense gas has also been invoked to explain reduced $[\text{O III}]\lambda\lambda 4959,5007$ emission in quasars (Temple et al. 2019; Wang et al. 2025).

Another well-known class of fast accretors that display weak $[\text{O III}]\lambda\lambda 4959,5007$ emission are the Narrow-Line Seyfert 1 galaxies (NLSy1; Osterbrock & Pogge 1985; Goodrich 1989).

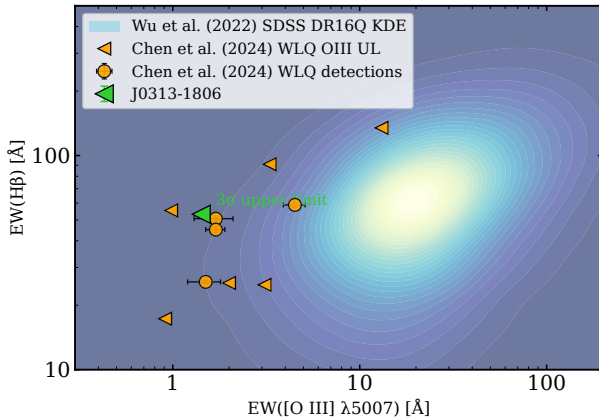


Fig. 6. Equivalent widths of $H\beta$ and upper limit on $[O\text{ III}]\lambda 5007$ for J0313-1806 (green triangle). We compare it to a sample of WLQs identified by (Chen et al. 2024) (orange circles for detected $[O\text{ III}]\lambda 5007$, orange triangles for upper limits). We also show Gaussian kernel density contours for SDSS DR16Q quasars (Wu & Shen 2022). This highlights the particular weakness of the $[O\text{ III}]\lambda\lambda 4959,5007$ emission in the nuclear spectrum of J0313-1806, even relative to typical WLQs.

However, we note that these objects are strictly classified based on their narrower $H\beta$ profiles ($< 2000 \text{ km s}^{-1}$), a criterion that is not met by J0313-1806.

5.1.2. J0313-1806 and the quasar main sequence

In addition to sharing characteristic WLQ properties, J0313-1806 is also a BAL quasar, indicative of strong outflows and/or shielding on nuclear scales. Such BAL features are extremely rare among WLQs (e.g., Nikołajuk & Walter 2012), with one other case reported by Yi et al. (2019). To anchor J0313-1806 in the EV1 context, we place it along the quasar main sequence (see, e.g., Marziani et al. 2018, for a review), in the primary EV1 plane defined by the FWHM of $H\beta$ and the relative strength of the optical Fe II emission, quantified as $r_{\text{FeII}} = F(\text{Fe II})/F(H\beta)$. For J0313-1806, we had obtained $\text{FWHM}(H\beta) = 4156 \pm 68 \text{ km s}^{-1}$ and compute $r_{\text{FeII}} = 0.95 \pm 0.13$. Archetypal quasar categories have been defined along this sequence (Sulentic et al. 2000), thought to be primarily driven by a combination of accretion rate (L/L_{Edd}) and the viewing angle toward a flattened BLR (e.g., Shen & Ho 2014). A canonical boundary at $\text{FWHM}(H\beta) \simeq 4000 \text{ km s}^{-1}$ separates rapidly accreting sources (Population A, $\text{FWHM}(H\beta) \lesssim 4000 \text{ km s}^{-1}$) from more massive, lower-accretion systems (Population B, $\text{FWHM}(H\beta) \gtrsim 4000 \text{ km s}^{-1}$) (e.g., Marziani et al. 2001). WLQs typically occupy the extreme Population A (xA) regime, characterized by $r_{\text{FeII}} \gtrsim 1$ (Diamond-Stanic et al. 2009; Martínez-Aldama et al. 2018; Dultzin et al. 2020).

In Fig. 7, we show the distribution of SDSS DR16Q quasars (Lyke et al. 2020; Wu & Shen 2022) in the redshift range $0.4 < z < 0.8$, selected following Shen & Ho (2014) with the criteria $0 < r_{\text{FeII}} < 3$, $\text{uni_flag} \neq 0$, $800 \text{ km s}^{-1} < \text{FWHM}(H\beta) < 15,000 \text{ km s}^{-1}$, and $\text{sn_flag} > 10$. The colour scale indicates the mean $\log_{10} \text{EW}([O\text{ III}])$ in bins of $\Delta r_{\text{FeII}} = 0.1$ and $\Delta \text{FWHM}(H\beta) = 500 \text{ km s}^{-1}$. We mark the position of J0313-1806 and overlay the WLQs presented by Chen et al. (2024), colour-coded by their measured or upper-limit $\text{EW}([O\text{ III}])$. J0313-1806 lies at the edge of the xA regime (formally $r_{\text{FeII}} > 1$). Several WLQs from Chen et al. (2024) also

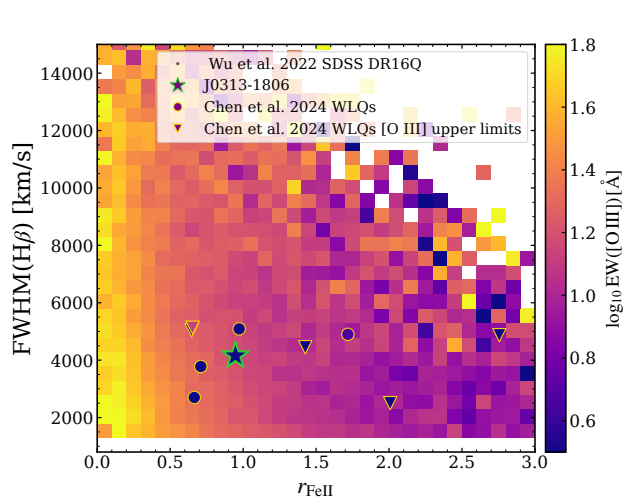


Fig. 7. EV1 plane $\text{FWHM}(H\beta)$ vs. r_{FeII} . The distribution of a subset of SDSS DR16Q quasars from Wu & Shen (2022) is shown in black (see text for selection criteria). The colourmap gives the mean $\log_{10} \text{EW}([O\text{ III}])$ in bins of size $\Delta r_{\text{FeII}} = 0.1$ and $\Delta \text{FWHM}(H\beta) = 500 \text{ km s}^{-1}$. J0313-1806 is shown as a green star. WLQs from Chen et al. (2024) are shown as circles (measured $\text{EW}([O\text{ III}]\lambda 5007)$) or triangles (upper limits), colour-coded according to their $\log_{10} \text{EW}([O\text{ III}])$. J0313-1806 and several WLQs lie outside the xA regime ($r_{\text{FeII}} > 1$) but nonetheless show strikingly weak $[O\text{ III}]\lambda 5007$ emission compared to SDSS DR16Q quasars in the same EV1 bins.

occupy a similar region of the plane. Notably, several of these objects exhibit $\text{EW}([O\text{ III}]\lambda 5007)$ values or limits that fall far below the typical SDSS DR16Q quasars in their local EV1 bins.

Quantitatively, the 3σ upper limit on $\text{EW}([O\text{ III}]\lambda 5007)$ for J0313-1806 is a factor of ~ 37 lower than the median value of SDSS DR16Q quasars at the same EV1 location ($\text{EW}([O\text{ III}]) = 15.76 \text{ Å}$, bin $0.90 \leq r_{\text{FeII}} < 1.00$ and $3800 \leq \text{FWHM}(H\beta) < 4300 \text{ km s}^{-1}$, containing 369 sources). This deficit corresponds to a one-sided percentile of $p = 3.8 \times 10^{-7}$, i.e. a 4.95σ outlier with respect to the local quasar population.

J0313-1806 exhibits exceptionally weak nuclear $[O\text{ III}]\lambda 5007$ emission compared to both the general quasar population at the same EV1 location and to local WLQs. This suggests that the extreme weakness of $[O\text{ III}]\lambda\lambda 4959,5007$ in J0313-1806 cannot be attributed solely to high- or super-Eddington accretion, but likely requires additional factors such as orientation, obscuration, or collisional de-excitation. In the paradigm presented by Shen & Ho (2014), at a fixed r_{FeII} , the spread in $\text{FWHM}(H\beta)$ primarily reflects orientation effects, with broader $\text{FWHM}(H\beta)$ corresponding to more edge-on viewing angles and narrower profiles to more face-on systems. For J0313-1806, our measured $\text{FWHM}(H\beta)$ and r_{FeII} place it among the broader $H\beta$ profile sources at this r_{FeII} (see black dots in Fig. 7), suggesting more edge-on configurations. Consequently, orientation alone is also unlikely to explain the unusually weak $[O\text{ III}]\lambda\lambda 4959,5007$ emission.

5.2. Suppressed extended $[O\text{ III}]$ emission

To further constrain the scenarios responsible for weak $[O\text{ III}]\lambda\lambda 4959,5007$ in J0313-1806 we will now discuss the kpc-scaled $H\beta$ emitting shell illuminated around the nucleus revealed in our JWST/NIRSpec IFU observation.

5.2.1. Photoionization simulations

In AGN, narrow-line emission can be observed out to kpc scales around the central continuum source (e.g., Bennert et al. 2002; Schmitt et al. 2003; Greene et al. 2011; Hainline et al. 2014; Liu et al. 2014). In quasar NLRs typical densities reach $n_e \sim 10^{2-4} \text{ cm}^{-3}$ (e.g., Bennert et al. 2006; Nagao et al. 2006; Kakkad et al. 2018; Joh et al. 2021), allowing forbidden high-ionization lines such as $[\text{O III}] \lambda\lambda 4959, 5007$ to be efficiently produced in partially ionized gas. This is not the picture observed in the extended emission around J0313–1806, where we report broadened $\text{H}\beta$ emission, with a median velocity dispersion of $\sigma = (415 \pm 51) \text{ km s}^{-1}$ but no significant $[\text{O III}] \lambda\lambda 4959, 5007$ in the immediate kpc-scale environment of the quasar. The observed peak in the $\text{H}\beta$ flux distribution suggests that the ionized shell is illuminated by the central source. The absence of $[\text{O III}] \lambda\lambda 4959, 5007$ emission throughout the shell is intriguing, and we explore potential physical scenarios to explain this in light of the simultaneous lack of nuclear $[\text{O III}] \lambda\lambda 4959, 5007$ emission (Sec. 5.1).

One of the leading physical explanations for the absence of $[\text{O III}] \lambda\lambda 4959, 5007$ in luminous quasars, as discussed in Section 5.1.2, is an orientation effect: the BLR outshines the NLR along low-inclination sightlines (e.g., Vietri et al. 2018). However, the complete absence of extended $[\text{O III}] \lambda\lambda 4959, 5007$ emission in the PSF-subtracted NIRSpec/IFU cube disfavors this interpretation for the shell. The extended and nuclear $[\text{O III}] \lambda\lambda 4959, 5007$ weakness must therefore be explained by the physical state of the gas and/or the ionizing SED rather than by orientation alone.

We carry out simulations with the python front-end `PyCLOUDY` (v0.9.15; Morisset 2013) and the `CLOUDY` photoionization code c23.01 (Ferland et al. 2013; Gunasekera et al. 2023), which computes the thermal, ionization, and line-emission structure of the shells.

Since $\text{H}\alpha \lambda 6563$, as well as the forbidden lines $[\text{N II}] \lambda 6583$ and $[\text{S II}] \lambda\lambda 6716, 6731$, lie outside the spectral window of our observations, and other diagnostic features such as the auroral $[\text{O III}] \lambda 4363$ line are too faint to be detected, we cannot apply standard emission line ratio diagnostics (e.g. Baldwin et al. 1981; Veilleux & Osterbrock 1987; Kauffmann et al. 2003; Kewley et al. 2006; Mazzolari et al. 2024; Scholtz et al. 2025). We use two primary diagnostic ratios: $\log_{10}([\text{O III}] 5007/\text{H}\beta)$ and $\log_{10}([\text{He II}] 4686/\text{H}\beta)$. We model a spherical shell of photoionized gas extending from $r_{\text{in}} \in \{0.1, 0.8, 1.7\} \text{ kpc}$ to $r_{\text{out}} = 1.8 \text{ kpc}$, with covering factor $C_f = 0.9$. The covering factor mimics an opening along our line of sight, exposing the BLR, as required by the observed nuclear broad $\text{H}\beta$. We note that varying C_f rescales the total line luminosities but leaves ratios unchanged to first order. The gas is dust-free, has constant density at the illuminated face, and is spherical (sphere). We vary metallicity over $\log(Z/Z_{\odot}) \in [-2.50, 0.25]$ in steps of 0.25 dex and density a wide range $\log n_{\text{H}}/\text{cm}^{-3} = \{3 - 8\}$ in steps of 0.5 dex. Metallicity-dependent elemental abundances are adopted following the analytic prescriptions of Nicholls et al. (2017, see also Decarli et al. 2024); in particular the oxygen abundance scales as

$$12 + \log(\text{O/H}) = 8.76 + \log Z, \quad (7)$$

with $\log Z$ the logarithmic metallicity relative to solar. We bracket the possible ionizing spectral shapes with two parameterized AGN continua using `CLOUDY`'s `agn` command. The rest-UV spectral slope is fixed by the spectrum in Wang et al. (2021): $\alpha_{\lambda} \simeq -0.91$ near $\text{Ly}\alpha$, which implies $\alpha_{\nu} = -(2 + \alpha_{\lambda}) = -1.09$. We therefore hold $\alpha_{\text{uv}} = -1.09$ in all models and vary only the

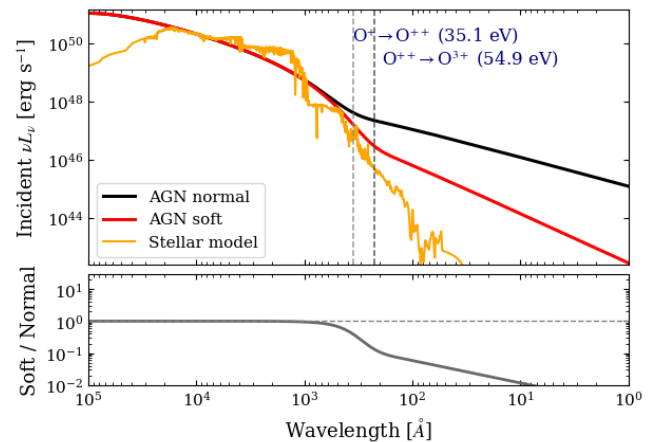


Fig. 8. AGN and stellar continuum models adopted in the `CLOUDY` simulations. *Upper panel*: The black line shows our "AGN normal" model with $T = 1.0 \times 10^5 \text{ K}$, $\alpha_{\text{uv}} = -1.09$, $\alpha_x = -1.0$ ($\Gamma \simeq 2.0$), and $\alpha_{\text{ox}} = -1.4$, representative of luminous quasars with typical X-ray emission. The red line shows our "AGN soft" model with $T = 1.0 \times 10^5 \text{ K}$, $\alpha_{\text{uv}} = -1.09$, $\alpha_x = -1.7$, and $\alpha_{\text{ox}} = -2.2$, chosen to mimic the steeper and X-ray–weaker spectra representative of WLQs. The orange line shows the BPASS starburst model. The vertical dashed lines indicate the ionization thresholds for $\text{O}^+ \rightarrow \text{O}^{++}$ (35.1 eV) and $\text{O}^{++} \rightarrow \text{O}^{3+}$ (54.9 eV). *Lower panel*: Ratio of the two continua, highlighting that the "AGN soft" model strongly suppresses the hard ionizing photon budget compared to the "AGN normal" case.

high-energy shape of the SEDs. Our "AGN normal" continuum adopts $T = 1.0 \times 10^5 \text{ K}$, $\alpha_{\text{uv}} = -1.09$, $\alpha_x = -1.0$ ($\Gamma \simeq 2.0$), and $\alpha_{\text{ox}} = -1.4$, representative of luminous quasars with standard X-ray output relative to their optical emission (Steffen et al. 2006; Just et al. 2007; Lusso et al. 2010; Nanni et al. 2017; Vito et al. 2019a). The "AGN soft" (WLQ-like) continuum instead has $T = 1.0 \times 10^5 \text{ K}$, $\alpha_{\text{uv}} = -1.09$, $\alpha_x = -1.7$, and $\alpha_{\text{ox}} = -2.2$, mimicking an extremely X-ray–weak quasar similar to observed WLQs (e.g., Luo et al. 2015; Timlin et al. 2020). Both continua are normalized to the observed optical luminosity $\nu L_{\nu}(5100 \text{ \AA}) = 1.77 \times 10^{46} \text{ erg s}^{-1}$, as derived in Section 3.1. The source models are shown in Fig. 8. Line emissivities are extracted per zone and integrated to total line powers. The $\text{O}^+ \rightarrow \text{O}^{++}$ ionization edge lies at 35.1 eV (354 Å); the suppression of photons above this threshold, like in our soft model naturally reduces the production of O^{++} and thus the strength of $[\text{O III}] \lambda\lambda 4959, 5007$ emission. However, in harder ionizing spectra, photons beyond the ionization edge at 54.9 eV ($\text{O}^{++} \rightarrow \text{O}^{3+}$) further ionize oxygen, generating O^{3+} and depleting $[\text{O III}] \lambda\lambda 4959, 5007$. We aim to test the net effect of the EUV-X-ray SEDs on the O^{++} ion population with our two models.

We further set up a "nuclear star formation" ionizing source model using a BPASS v2.2.1 (Eldridge et al. 2017; Stanway & Eldridge 2018) spectrum corresponding to a 10 Myr instantaneous burst at solar metallicity (orange line in Fig. 8). The spectrum was normalized to a total ionizing photon output of $\log_{10} Q(\text{H}) \sim 50$, consistent with a vigorous nuclear starburst producing several $\times 10^2 M_{\odot} \text{ yr}^{-1}$ (e.g., Kennicutt 1998) typical of luminous $z \sim 7$ quasar hosts. We stress, however, that the quasar should overwhelmingly dominate the ionizing photon budget. Nuclear star-formation is included only as a comparison case to illustrate the ionization conditions expected in the absence of a hard AGN spectrum, rather than as a realistic alternative single power source.

In Fig. 9 we show the simulated line ratios $\log_{10}([\text{O III}] 5007/\text{H}\beta)$ across grids of hydrogen density n_{H} and metallicity Z for the AGN normal", "AGN soft" and stellar models, each evaluated at three inner shell radii $r_{\text{in}} \in 0.1, 0.8, 1.7 \text{ kpc}$. Regions where $\log_{10}([\text{O III}] 5007/\text{H}\beta) < -1.15$ (Section 4.2) are highlighted as consistent with the ratio measured in the integrated spectrum of the shell. The illuminated skin of an AGN-irradiated shell is expected to be compressed until the gas pressure balances the incident radiation pressure—so-called radiation-pressure confinement (RPC; e.g., Draine 2011; Stern et al. 2014a,b; Baskin et al. 2014a,b; Baskin & Laor 2021). This sets a characteristic density floor, $n_{\text{floor}} \sim P_{\text{rad}}/(kT) \approx L/(4\pi r^2 c kT)$. We do not enforce an RPC in our Cloudy models; densities below this floor are shown for completeness but are treated as physically disfavoured. Figure 9 shows the corresponding "RPC exclusion zone." Cosmological zoom-in simulations (Costa et al. 2015) indicate that cold gas can further be pressure-confined by a hot, volume-filling shocked medium (see also Stern et al. 2016). Even if this hot phase remains undetected in our IFU data, it would only add to the total pressure, so the RPC floor remains a valid lower bound.

We see only minor differences between the "AGN normal" and "AGN soft" continuum-driven runs in terms of the accessible parameter space, with slightly lower densities accessible in the "AGN soft" model. This indicates that, assuming AGN photoionization, the depletion of $[\text{O III}] \lambda\lambda 4959, 5007$ is primarily driven by collisional de-excitation or metallicity rather than by spectral hardness. For all three inner radii probed, there exist regions of parameter space that are consistent with the observational constraint $\log_{10}([\text{O III}] 5007/\text{H}\beta) < -1.15$, as well as regions that are inconsistent. To first order, our models show that reproducing the observed weakness of $[\text{O III}] \lambda\lambda 4959, 5007$ requires either very high gas densities ($n_{\text{H}} \gtrsim 10^6 \text{ cm}^{-3}$, where collisional suppression becomes efficient independent of metallicity) or, at lower densities ($n_{\text{H}} \lesssim 10^5 \text{ cm}^{-3}$), sub-solar metallicities ($Z \lesssim 0.2 Z_{\odot}$). Thus, both high-density and low-metallicity solutions are supported.

At very high densities, $n_{\text{H}} \gtrsim 10^7 \text{ cm}^{-3}$, collisional de-excitation is so efficient that the observed ratios can be reproduced almost irrespective of metallicity or shell thickness. At densities $n_{\text{H}} \sim 10^{5-7} \text{ cm}^{-3}$, the line ratios are increasingly suppressed with decreasing metallicity, $Z \lesssim 0.1-0.2 Z_{\odot}$. For more moderate densities, $n_{\text{H}} \lesssim 10^{4.5} \text{ cm}^{-3}$, the predicted ratios exceed the observed limit across essentially the entire metallicity range. A thinner shell, i.e. with a larger inner radius (e.g. $r_{\text{in}} = 1.7 \text{ kpc}$) significantly relaxes the density requirements, enabling $n_{\text{H}} \sim 10^5 \text{ cm}^{-3}$.

The even softer "nuclear star formation" SED enables access to consistent $\log_{10}([\text{O III}] 5007/\text{H}\beta)$ ratios over a larger set of density and metallicity combinations, with $n_{\text{H}} \sim 10^4 \text{ cm}^{-3}$ densities available up to $\log(Z/Z_{\odot}) \sim 1$.

We note, however, that even for the lower possible densities $n_{\text{H}} \gtrsim 10^{3.5} \text{ cm}^{-3}$, the total gas mass implied by a uniform, kpc-scale shell becomes unrealistically large. The ionized gas mass of a shell with inner radius r_{in} , outer radius r_{out} , covering factor C_f , and filling factor f is:

$$M_{\text{gas}} \approx 4\pi C_f f \mu m_p n_{\text{H}} (r_{\text{out}}^3 - r_{\text{in}}^3)/3, \quad (8)$$

where $\mu \approx 1.4$ is the mean particle mass per hydrogen nucleus.

Considering the optimistic case of a thin shell with $r_{\text{in}} \sim 1.7 \text{ kpc}$, a shell thickness of 100 pc, $C_f = 0.9$ and $n_{\text{H}} \sim 10^{3.5} \text{ cm}^{-3}$,

this expression yields $M_{\text{gas}} \sim 1.3 \times 10^{11} M_{\odot}$ if the gas is volume-filling, i.e., $f = 1$. Such a mass is implausibly large for kpc-scale gas reservoirs in early galaxies. Compared to observational constraints from dust and $[\text{C II}] \lambda 157.6 \mu\text{m}$ ($M_{\text{dust}} \sim 7 \times 10^7 M_{\odot}$, Wang et al. 2021) this would require unreasonably high gas-to-dust ratios (realistic gas-to-dust ratios are of the 10^2 , e.g., Li et al. 2019). The dense phase required to collisionally quench $[\text{O III}] \lambda\lambda 4959, 5007$ cannot be distributed in a volume-filling layer. Instead, the emitting material must occupy only a small fraction of the swept-up volume, implying a low filling factor ($f \lesssim 0.05$) to keep the total ionized mass within reasonable bounds. One plausible realization is emission from dense clumps or a thin layer within the shell, but other geometries with similarly low filling factors cannot be excluded. We are assuming a spherical symmetric shell for simplicity, while the observed distribution is also consistent with a partial shell (or even more complex geometry), which would allow us to reduce the total gas mass by a factor of up to ~ 10 .

Our observed upper limit in $[\text{O III}]/\text{H}\beta$ ratios is thus consistent with ionization from an AGN or nuclear star formation, only if we assume a clumpy geometry for the shell. In Section 4, we also derived an upper limit on a second line ratio: $[\log_{10}(\frac{F([\text{He II}])}{F(\text{H}\beta)})]_{<3\sigma} = -1.12$. This ratio is primarily sensitive to the hardness of the ionizing radiation field and can be used to distinguish between AGN- and star formation–driven photoionization scenarios (e.g. Decarli et al. 2024). However, when comparing our 3σ upper limit to the simulation results presented by Decarli et al. (2024, see their Fig. 9), we find that our measurement does not allow us to conclusively differentiate between the two photoionization scenarios. We, however, note that a soft ionizing continuum such as the one from nuclear star-formation model would significantly relax the density, thickness, and filling-factor requirements.

5.2.2. $\text{H}\beta$ shell energetics

Following Osterbrock & Ferland (2006) (see also Vayner et al. 2024; Liu et al. 2024), the recombination mass of the spatially resolved $\text{H}\beta$ shell contained in each spaxel can be calculated as:

$$M_{\text{ion}}^{ij} = \frac{m_p L_{\text{H}\beta}^{ij}}{\alpha_{\text{H}\beta} h v_{\text{H}\beta} n_e}, \quad (9)$$

where m_p is the mass of the proton, $L_{\text{H}\beta}$ the luminosity of $\text{H}\beta$, $\alpha_{\text{H}\beta}$ is the effective $\text{H}\beta$ recombination coefficient, h is the Planck constant, $v_{\text{H}\beta}$ is the restframe frequency of $\text{H}\beta$ and n_e is the electron density. Here we assume that $\text{H}\beta$ is mainly produced through recombination and model the emitting gas as an ensemble of identical, unresolved gas elements (hereafter referred to as "clouds"). Each cloud has a fixed electron density. Assuming Case B recombination, we calculate the recombination coefficient of $\text{H}\beta$ using the nebular emission line analysis package `pyneb` (Luridiana et al. 2015). We note that the recombination mass is formally different than the total gas mass calculated in Eq. 9, as it only traces the HII region actively emitting $\text{H}\beta$.

We consider conditions similar to the ones supported by our Cloudy AGN simulations and set $n_e = 10^6 \text{ cm}^{-3}$ ($\alpha_{\text{H}\beta} = 3.071 \times 10^{-14} \text{ cm}^{-3} \text{ s}^{-1}$) and fix the temperature to $T = 10^4 \text{ K}$. These numbers yield a total recombination mass of $M_{\text{ion},\text{tot}} = (1.02 \pm 0.09) \times 10^3 M_{\odot}$ for the shell.

We can then compute integrated and instantaneous energetics of the outflow. We start by the integrated ionized mass outflow rate:

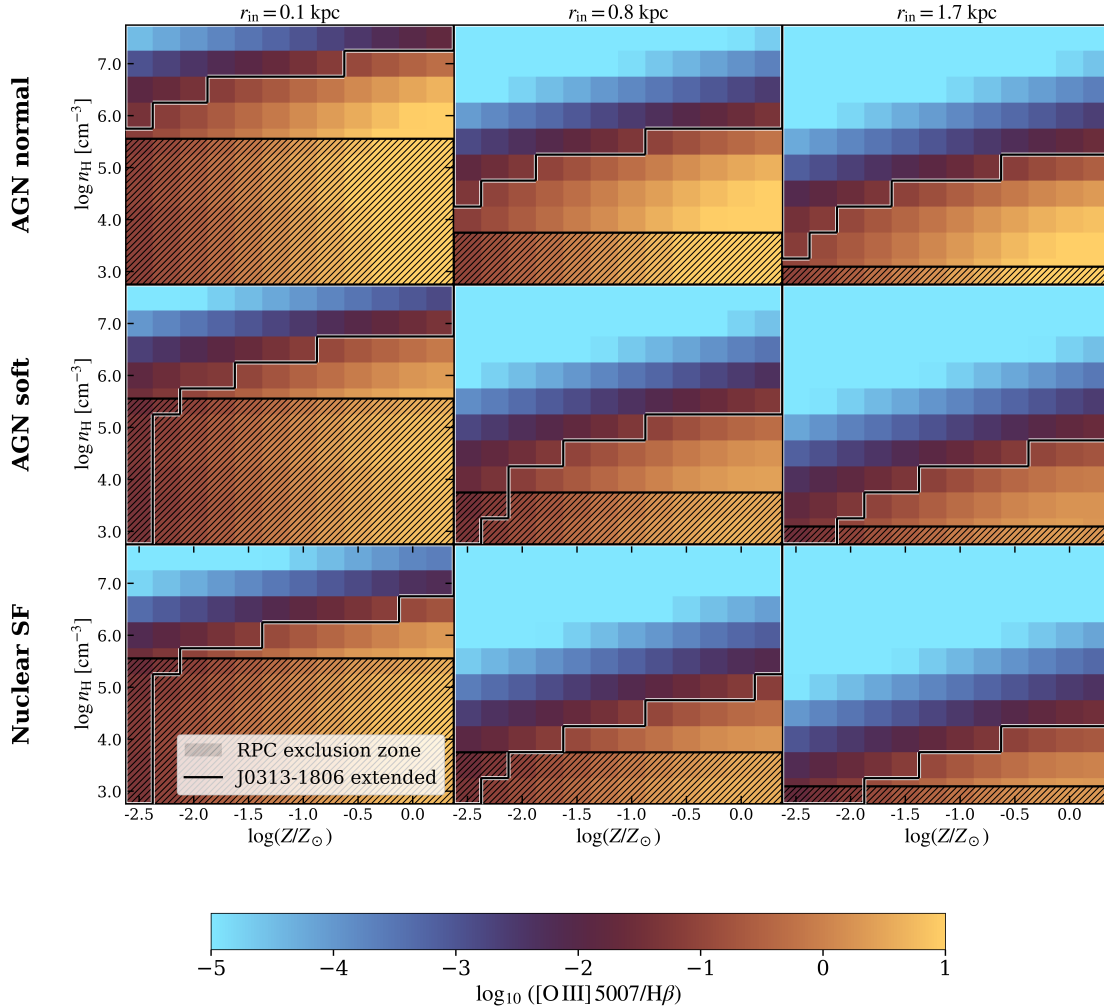


Fig. 9. Cloudy simulation results for the $\text{H}\beta$ shell. The upper and middle rows correspond to models using the “AGN normal” and AGN soft” continua as ionizing sources, respectively, while the lower row corresponds to the stellar ionizing source. Each panel shows the predicted line ratio $\log_{10}([\text{O III}] 5007/\text{H}\beta)$ as a function of gas density n_{H} and metallicity Z , for inner shell radii $r_{\text{in}} = 0.1, 0.8$, and 1.7 kpc (left to right). The maps are spanned by constant-density shell models with outer radius $r_{\text{out}} = 1.8$ kpc. Regions enclosed by the black contour are consistent with the observed constraint $\log_{10}([\text{O III}]/\text{H}\beta) < -1.15$ from the extended emission in J0313-1806. The hatched areas indicate the radiation–pressure confinement (RPC) exclusion zone, where densities fall below the expected RPC floor and are therefore disfavored.

$$\dot{M}_{\text{ion}}^{\text{int}} = \sum_{ij} \frac{M_{\text{ion}}^{ij} v_{\text{out}}^{ij}}{R^{ij}}, \quad (10)$$

where $v_{\text{out}}^{ij} = |v_{50}^{ij}| + \sigma^{ij}$ is the outflow velocity, i.e. the sum of the absolute velocity offset traced by the non-parametric v_{50} and the velocity dispersion. This convention allows us to capture the maximum outflow velocity encoded in the winds of the emission line (Rupke & Veilleux 2013; Vayner et al. 2024). R^{ij} represents the physical projected distance between the spaxel (i, j) and the quasar coordinates (49,46). Following Vayner et al. (2024) we also obtain the spaxel-wise instantaneous mass outflow rate from:

$$\dot{M}_{\text{ion}}^{ij} = \frac{M_{\text{ion}}^{ij} v_{\text{out}}^{ij}}{dR}, \quad (11)$$

where dR is the physical size of a single spaxel. We further calculate integrated and instantaneous momentum and kinetic luminosities using the following equations:

$$\dot{P}_{\text{ion}}^{ij} = M_{\text{ion}}^{ij} v^{ij} \quad E_{\text{kin,ion}}^{ij} = \frac{1}{2} M_{\text{ion}}^{ij} (v^{ij})^2 \quad (12)$$

In the absence of a significant detection of $\text{H}\gamma$ in the PSF-subtracted cube, we can only place an upper limit on the flux ratio $F(\text{H}\gamma)/F(\text{H}\beta)$ by considering spaxels with robust $\text{H}\beta$ detections ($\text{S/N}_{\text{H}\beta} > 3$). The resulting limits yield a median constraint of $F(\text{H}\gamma)/F(\text{H}\beta) < 0.44$. This limit is only slightly lower than the theoretical Case B recombination value of $F(\text{H}\gamma)/F(\text{H}\beta) = 0.47$ for $T_{\text{e}} = 10^4$ K and $n_{\text{e}} = 100$ cm $^{-3}$, and therefore does not provide a meaningful constraint on the reddening. We therefore do not apply an extinction correction to the $\text{H}\beta$ flux, noting that any unaccounted extinction would increase the inferred line luminosity and associated energetics.

Following Vayner et al. (2024), we also measure the median instantaneous energetics in concentric shells around the quasar position with a radius increment of 0.3 kpc. Our integrated and cumulative measurements are shown in Fig. 10. We find that the median instantaneous outflow velocity v_{out} increases with radius, reaching 600–700 km s $^{-1}$ at ~ 1.1 kpc and remaining high at larger radii. The overall median value of 377 ± 85 km s $^{-1}$ is lower

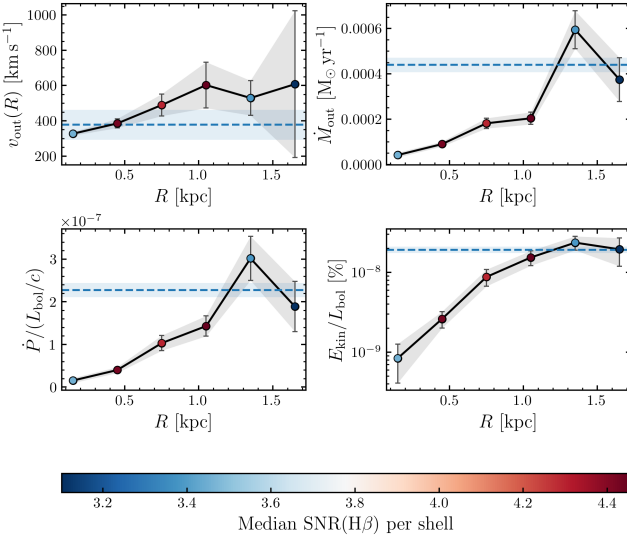


Fig. 10. $H\beta$ spatially resolved energetics. Here we show the median values of the instantaneous energetics calculated in concentric shells centred on the quasar (circles) and their associated 1σ uncertainties. The points are colour-coded by median $S/N_{H\beta}$ in that shell. The upper right panel shows the outflow velocity, the upper right one shows the mass outflow rate, the lower right one the momentum flux ratio and the lower right one the energy flux ratio. The horizontal lines and shaded areas represent the corresponding integrated measurements and their 1σ uncertainties. For v_{out} we show the median velocity and the median absolute deviation.

than the median instantaneous velocities measured beyond 1 kpc, showing that a subset of outer pixels drives the fastest outflows and dominates the kinematics. The instantaneous mass outflow rate \dot{M}_{out} and the momentum flux \dot{P} also rise toward larger radii, and their localized peak is consistent with a thin-shell geometry.

Assuming a high gas density of $n_{\text{H}} = 10^6 \text{ cm}^{-3}$, the outflow rates remain modest, with an integrated value of $\dot{M}_{\text{ion}}^{\text{int}} = (4.3 \pm 0.3) \times 10^{-4} M_{\odot} \text{ yr}^{-1}$. The corresponding integrated momentum flux is low, $\dot{P}_{\text{ion}}^{\text{int}}/(L_{\text{bol}}/c) = (2.3 \pm 0.2) \times 10^{-7} \ll 1$, showing that the outflow is strongly momentum starved compared to the quasar luminosity. The kinetic power of the outflow, both instantaneous and integrated, increases smoothly with radius but remains far below the percent-level energy coupling typically associated with quasar feedback, demonstrating that it is energetically negligible.

The narrow radial localization of the maximum velocity and mass outflow rate supports the geometry of a thin expanding shell. The very low efficiency relative to L_{bol} suggests that the observed ionized component may represent only a thin skin on the surface of a much larger neutral or molecular outflow that is not traced with the NIRSpec/IFU data. The low coupling efficiency might suggest that the driving phase of this outflow has ended, i.e., that it is a fossil remnant of dense gas pushed out earlier in the quasar lifecycle. Assuming a maximum outflow velocity of $\sim 600 \text{ km s}^{-1}$ and a radius of roughly 2 kpc, we obtain $t_{\text{dyn}} \sim 3 \text{ Myr}$, setting a rough timescale for a potential blowout event. High-resolution imaging of the cold molecular phase could reveal whether the ionized outflow is indeed the membrane of a larger molecular region carrying more mass and momentum.

5.3. Obscured black hole growth and fossil evidence for blowout phase

The recent JWST discovery of high-redshift AGN exhibiting extreme Balmer breaks (e.g., de Graaff et al. 2025; Naidu et al. 2025) has prompted the development of models of black hole growth deeply embedded in extremely dense gas envelopes (e.g., Inayoshi & Maiolino 2025; Rusakov et al. 2025; Kido et al. 2025). These models naturally account for the observed SED shapes without invoking stellar populations.

These findings support the early super-Eddington growth of black holes embedded in dense gas reservoirs (e.g. Volonteri & Begelman 2010). If such an enshrouded phase of black hole growth exists, it must be incorporated into the overall AGN evolutionary cycle and linked to the subsequent luminous quasar phase. Simulations by Lupi et al. (2024a); Huško et al. (2025) support this type of evolutionary phase. Feedback processes are expected to clear out or consume the surrounding gas during a brief blowout stage (e.g. Zakamska et al. 2016; Vayner et al. 2025). In cosmological zoom-in simulations presented by Quadri et al. (2025) the strong feedback event punctuating the rapid accretion phase of SMBHs are followed by a transient quenched phase.

Quasars are indeed expected to undergo most of their early growth phases enshrouded in dust and gas (Jahnke 2025), with $> 82\%$ predicted to be obscured at $z > 7$ (e.g., Davies et al. 2019). The recent discovery of blazars at $z \sim 7$ provides further support for prolonged obscured growth phases in early SMBHs (Belladitta et al. 2020; Wolf et al. 2024; Ighina et al. 2024; Bañados et al. 2025b).

Dust obscuration by a nuclear parsec-scale distribution is a key ingredient in the AGN unification model (Urry & Padovani 1995; Netzer 2015, for reviews). However, the increase of cold gas content in the interstellar medium (ISM) with redshift (e.g., Scoville et al. 2017; Tacconi et al. 2018) and the simultaneous overall decrease of galaxy sizes (e.g., Allen et al. 2017; Miller 2007) toward earlier cosmic time has motivated models in which the dense ISM itself can act as an effective obscuring screen (Gilli et al. 2022). Indeed, combining ALMA and *Chandra* observations of Compton-thick quasars, Gilli et al. (2014); Circosta et al. (2019); D’Amato et al. (2020) linked the observed X-ray absorption to the high ISM column densities in their host galaxies.

Our analysis provides evidence for a thin, clumpy, energetically decoupled ionized shell surrounding J0313–1806. One possible interpretation is that this shell is the fossil signature of a recent clearing feedback event (i.e., a blowout), consistent with the strong nuclear outflows reported in the unresolved central region (Wang et al. 2021). The WLQ-like nuclear properties of J0313–1806, in particular the observed $[\text{O III}] \lambda\lambda 4959, 5007$ depletion, are therefore unlikely to be driven primarily by the ionizing continuum shape or orientation. Instead, we propose that the density of the irradiated (and recently expelled) gas slab drives the collisional de-excitation of $[\text{O III}] \lambda\lambda 4959, 5007$.

Interestingly, the only two other quasars currently known at $z \sim 7.5$, J100758.26+211529.2 (Yang et al. 2020; Liu et al. 2024) and ULAS J134208.10+092838.61 (Bañados et al. 2018; Trefoloni et al. 2025), also exhibit relatively weak $[\text{O III}] \lambda\lambda 4959, 5007$ emission and similar $H\beta$ line profiles in their restframe optical nuclear spectra observed with JWST/NIRSpec IFU. This raises the question of whether similar physical processes operate on their nuclear scales as in J0313–1806, and whether they might likewise host dense, clumpy ionized gas distributions on kiloparsec scales that link WLQ-like

behaviour to the obscured phases of quasar evolution. However, the situation may be more complex, as both of these quasars also show kpc-scale [O III] $\lambda\lambda 4959, 5007$ emission (Liu et al. 2024; Trefoloni et al. 2025), unlike J0313–1806.

6. Conclusions

Our JWST/NIRSpec IFU observations of J0313–1806, the most distant currently known quasar at $z = 7.6423$, reveal intriguing nuclear and extended (kpc scale) properties. Our findings show that J0313–1806 is a rare BAL WLQ with extraordinarily weak [O III] $\lambda\lambda 4959, 5007$ emission. More remarkably, we discovered an extended ionized gas shell spanning kpc scales that completely lacks [O III] $\lambda\lambda 4959, 5007$ emission yet shows clear H β . The ordered kinematics of this shell are energetically decoupled from the quasar’s bolometric output and are likely not driven by ongoing feedback. Our data are consistent with a thin, clumpy-shell geometry, which we interpret as a fossil remnant of a recent blowout phase in the context of obscured black hole growth. If correct, the uncovered shell could represent the ionized skin of a much more massive, cold gas layer.

This interpretation suggests that typical properties of WLQs across cosmic time—[O III] $\lambda\lambda 4959, 5007$ and X-ray weakness—can be explained by extremely dense interstellar gas with high column densities, which suppresses high-ionization emission lines via collisional de-excitation while absorbing the X-ray emission. In this picture, WLQs represent a transitional stage in which recently cleared, dense, clumpy ISM gas still regulates the observed quasar spectral properties.

Recent support for this scenario comes from Ďurovčíková et al. (2025), who presented NIRSpec IFU spectroscopy of the $z = 5.9$ WLQ SDSS J1335+3533. Similar to J0313–1806, its nuclear spectrum exhibits weak [O III] $\lambda\lambda 4959, 5007$ emission potentially blended with the Fe II pseudo-continuum, and shows a pronounced weakness of extended [O III] $\lambda\lambda 4959, 5007$ emission relative to Balmer lines. These striking similarities suggest that the phenomena we observe in J0313–1806 may represent a broader evolutionary phase in quasar-host co-evolution.

J0313–1806 thus provides an unprecedented view into SMBH-host coevolution at cosmic dawn, establishing a framework for understanding WLQ properties that can now be tested with systematic JWST IFU surveys of early quasars.

Acknowledgements. J.W. gratefully acknowledges Hannah Übler for insightful discussions on integral-field spectroscopy at high redshift, and Chris Done for valuable guidance on weak-line quasars and line-driven outflows.

C.M. acknowledges support from Fondecyt Iniciacion grant 11240336 and the ANID BASAL project FB210003.

D.S.N.R. was supported under program #DD-ERS-1335 through a grant from the Space Telescope Science Institute, which is operated by the Association of Universities for Research in Astronomy, Inc., under NASA contract NAS 5-03127. J.-T.S. is supported by the Deutsche Forschungsgemeinschaft (DFG, German Research Foundation) - Project number 518006966.

B.T. acknowledges support from the European Research Council (ERC) under the European Union’s Horizon 2020 research and innovation program (grant agreement number 950533), and by the Excellence Cluster ORIGINS which is funded by the Deutsche Forschungsgemeinschaft (DFG, German Research Foundation) under Germany’s Excellence Strategy - EXC 2094 - 390783311.

RD acknowledges support from the INAF GO 2022 grant “The birth of the giants: JWST sheds light on the build-up of quasars at cosmic dawn”, the INAF mini-grant 2024: “The interstellar medium at high redshift”, and the PRIN MUR “2022935STW”, RFF M4.C2.1.1, CUP J53D23001570006 and C53D23000950006.

This work is based on observations made with the NASA/ESA/CSA James Webb Space Telescope. The data were obtained from the Mikulski Archive for Space Telescopes at the Space Telescope Science Institute, which is operated by the Association of Universities for Research in Astronomy, Inc., under NASA contract NAS 5-03127 for JWST. These observations are associated with program #1764.

The data underlying this article are available from the Mikulski Archive for Space Telescopes (MAST) at <https://doi.org/10.17909/0qd3-x220>. Funding for the Sloan Digital Sky Survey IV has been provided by the Alfred P. Sloan Foundation, the U.S. Department of Energy Office of Science, and the Participating Institutions. SDSS-IV acknowledges support and resources from the Center for High Performance Computing at the University of Utah. The SDSS website is www.sdss4.org. SDSS-IV is managed by the Astrophysical Research Consortium for the Participating Institutions of the SDSS Collaboration including the Brazilian Participation Group, the Carnegie Institution for Science, Carnegie Mellon University, Center for Astrophysics | Harvard & Smithsonian, the Chilean Participation Group, the French Participation Group, Instituto de Astrofísica de Canarias, The Johns Hopkins University, Kavli Institute for the Physics and Mathematics of the Universe (IPMU) / University of Tokyo, the Korean Participation Group, Lawrence Berkeley National Laboratory, Leibniz Institut für Astrophysik Potsdam (AIP), Max-Planck-Institut für Astronomie (MPIA Heidelberg), Max-Planck-Institut für Astrophysik (MPA Garching), Max-Planck-Institut für Extraterrestrische Physik (MPE), National Astronomical Observatories of China, New Mexico State University, New York University, University of Notre Dame, Observatório Nacional / MCTI, The Ohio State University, Pennsylvania State University, Shanghai Astronomical Observatory, United Kingdom Participation Group, Universidad Nacional Autónoma de México, University of Arizona, University of Colorado Boulder, University of Oxford, University of Portsmouth, University of Utah, University of Virginia, University of Washington, University of Wisconsin, Vanderbilt University, and Yale University. Collaboration Overview Affiliate Institutions Key People in SDSS Collaboration Council Committee on Inclusiveness Architects SDSS-IV Survey Science Teams and Working Groups Code of Conduct SDSS-IV Publication Policy How to Cite SDSS External Collaborator Policy For SDSS-IV Collaboration Members

This work made use of Astropy:⁶ a community-developed core Python package and an ecosystem of tools and resources for astronomy (Astropy Collaboration et al. 2013, 2018, 2022).

This work made use of v2.2.1 of the Binary Population and Spectral Synthesis (BPASS) models as described in Eldridge et al. (2017) and Stanway & Eldridge (2018).

We thank the referee for a careful review of the manuscript and for constructive comments that improved the clarity and robustness of this work.

References

Abramowicz, M. A. 2005, in *Growing Black Holes: Accretion in a Cosmological Context*, ed. A. Merloni, S. Nayakshin, & R. A. Sunyaev, 257–273

Abramowicz, M. A., Czerny, B., Lasota, J. P., & Szuszkiewicz, E. 1988, *ApJ*, 332, 646

Allen, R. J., Kacprzak, G. G., Glazebrook, K., et al. 2017, *ApJ*, 834, L11

Assef, R. J., Eisenhardt, P. R. M., Stern, D., et al. 2015, *ApJ*, 804, 27

Astropy Collaboration, Price-Whelan, A. M., Lim, P. L., et al. 2022, *ApJ*, 935, 167

Astropy Collaboration, Price-Whelan, A. M., Sipőcz, B. M., et al. 2018, *AJ*, 156, 123

Astropy Collaboration, Robitaille, T. P., Tollerud, E. J., et al. 2013, *A&A*, 558, A33

Bañados, E., Le Brun, V., Belladitta, S., et al. 2025a, *MNRAS*, 542, 1088

Bañados, E., Momjian, E., Connor, T., et al. 2025b, *Nature Astronomy*, 9, 293

Bañados, E., Schindler, J.-T., Venemans, B. P., et al. 2023, *ApJS*, 265, 29

Bañados, E., Venemans, B. P., Decarli, R., et al. 2016, *ApJS*, 227, 11

Bañados, E., Venemans, B. P., Mazzucchelli, C., et al. 2018, *Nature*, 553, 473

Baldwin, J. A. 1977, *ApJ*, 214, 679

Baldwin, J. A., Phillips, M. M., & Terlevich, R. 1981, *PASP*, 93, 5

Baskin, A. & Laor, A. 2005, *MNRAS*, 358, 1043

Baskin, A. & Laor, A. 2021, *MNRAS*, 508, 680

Baskin, A., Laor, A., & Stern, J. 2014a, *MNRAS*, 438, 604

Baskin, A., Laor, A., & Stern, J. 2014b, *MNRAS*, 445, 3025

Belladitta, S., Bañados, E., Xie, Z.-L., et al. 2025, *A&A*, 699, A335

Belladitta, S., Moretti, A., Caccianiga, A., et al. 2020, *A&A*, 635, L7

Bennert, N., Falcke, H., Schulz, H., Wilson, A. S., & Wills, B. J. 2002, *ApJ*, 574, L105

Bennert, N., Jungwiert, B., Komossa, S., Haas, M., & Chini, R. 2006, *A&A*, 459, 55

Böker, T., Arribas, S., Lützgendorf, N., et al. 2022, *A&A*, 661, A82

Boroson, T. A. & Green, R. F. 1992, *ApJS*, 80, 109

Buchner, J., Georgakakis, A., Nandra, K., et al. 2015, *ApJ*, 802, 89

Castor, J. I., Abbott, D. C., & Klein, R. I. 1975, *ApJ*, 195, 157

Chen, Y., Luo, B., Brandt, W. N., et al. 2024, *ApJ*, 972, 191

Circosta, C., Vignali, C., Gilli, R., et al. 2019, *A&A*, 623, A172

⁶ <http://www.astropy.org>

Costa, T., Sijacki, D., & Haehnelt, M. G. 2015, MNRAS, 448, L30

D'Amato, Q., Gilli, R., Vignali, C., et al. 2020, A&A, 636, A37

Davies, F. B., Hennawi, J. F., & Eilers, A.-C. 2019, ApJ, 884, L19

de Graaff, A., Rix, H.-W., Naidu, R. P., et al. 2025, A&A, 701, A168

Decarli, R., Loiacono, F., Farina, E. P., et al. 2024, A&A, 689, A219

Diamond-Stanic, A. M., Fan, X., Brandt, W. N., et al. 2009, ApJ, 699, 782

Ding, X., Onoue, M., Silverman, J. D., et al. 2023, Nature, 621, 51

Ding, X., Silverman, J. D., & Onoue, M. 2022, ApJ, 939, L28

Draine, B. T. 2011, ApJ, 732, 100

Dultzin, D., Marziani, P., de Diego, J. A., et al. 2020, Frontiers in Astronomy and Space Sciences, 6, 80

Dumont, A., Neumayer, N., Seth, A. C., et al. 2025, A&A, 703, A54

Eilers, A.-C., Simcoe, R. A., Yue, M., et al. 2023, ApJ, 950, 68

Eldridge, J. J., Stanway, E. R., Xiao, L., et al. 2017, PASA, 34, e058

Fan, X., Bañados, E., & Simcoe, R. A. 2023, ARA&A, 61, 373

Fan, X., Narayanan, V. K., Lupton, R. H., et al. 2001, AJ, 122, 2833

Fan, X., Strauss, M. A., Gunn, J. E., et al. 1999, ApJ, 526, L57

Farina, E. P., Schindler, J.-T., Walter, F., et al. 2022, ApJ, 941, 106

Ferland, G. J., Porter, R. L., van Hoof, P. A. M., et al. 2013, Rev. Mexicana Astron. Astrofis., 49, 137

Ferrarese, L. & Merritt, D. 2000, ApJ, 539, L9

Foroosh, H., Zerubia, J., & Berthod, M. 2002, IEEE Transactions on Image Processing, 11, 188

Gardner, J. P., Mather, J. C., Clampin, M., et al. 2006, Space Sci. Rev., 123, 485

Gebhardt, K., Kormendy, J., Ho, L. C., et al. 2000, ApJ, 543, L5

Gilli, R., Norman, C., Calura, F., et al. 2022, A&A, 666, A17

Gilli, R., Norman, C., Vignali, C., et al. 2014, A&A, 562, A67

Glikman, E., Lacy, M., LaMassa, S., et al. 2018, ApJ, 861, 37

Gloudemans, A. J., Duncan, K. J., Saxena, A., et al. 2022, A&A, 668, A27

Goodrich, R. W. 1989, ApJ, 342, 224

Greene, J. E. & Ho, L. C. 2005, ApJ, 630, 122

Greene, J. E., Zakamska, N. L., Ho, L. C., & Barth, A. J. 2011, ApJ, 732, 9

Gunasekera, C. M., van Hoof, P. A. M., Chatzikos, M., & Ferland, G. J. 2023, Research Notes of the American Astronomical Society, 7, 246

Guo, H., Shen, Y., & Wang, S. 2018, PyQSOFit: Python code to fit the spectrum of quasars, Astrophysics Source Code Library, record ascl:1809.008

Ha, T., Dix, C., Matthews, B. M., et al. 2023, ApJ, 950, 97

Habouzit, M., Li, Y., Somerville, R. S., et al. 2021, MNRAS, 503, 1940

Hainline, K. N., Hickox, R. C., Greene, J. E., et al. 2014, ApJ, 787, 65

Häring, N. & Rix, H.-W. 2004, ApJ, 604, L89

Hewett, P. C., Warren, S. J., Leggett, S. K., & Hodgkin, S. T. 2006, MNRAS, 367, 454

Hopkins, P. F., Hernquist, L., Cox, T. J., et al. 2006, ApJS, 163, 1

Huško, F., Lacey, C. G., Roper, W. J., et al. 2025, MNRAS, 537, 2559

Ighina, L., Caccianiga, A., Moretti, A., et al. 2024, arXiv e-prints, arXiv:2407.04094

Inayoshi, K. & Maiolino, R. 2025, ApJ, 980, L27

Inayoshi, K., Visbal, E., & Haiman, Z. 2020, ARA&A, 58, 27

Ishibashi, W., Fabian, A. C., & Arakawa, N. 2021, MNRAS, 502, 3638

Ishibashi, W., Fabian, A. C., Ricci, C., & Celotti, A. 2018, MNRAS, 479, 3335

Ishikawa, Y., Zakamska, N. L., Shen, Y., et al. 2025, ApJ, 982, 22

Iwasawa, K., Comastri, A., Vignali, C., et al. 2020, A&A, 639, A51

Jahnke, K. 2025, The Open Journal of Astrophysics, 8, 9

Jiang, L., McGreer, I. D., Fan, X., et al. 2016, ApJ, 833, 222

Joh, K., Nagao, T., Wada, K., Terao, K., & Yamashita, T. 2021, PASJ, 73, 1152

Just, D. W., Brandt, W. N., Shemmer, O., et al. 2007, ApJ, 665, 1004

Kakkad, D., Groves, B., Dopita, M., et al. 2018, A&A, 618, A6

Kaspi, S., Smith, P. S., Netzer, H., et al. 2000, ApJ, 533, 631

Kauffmann, G., Heckman, T. M., Tremonti, C., et al. 2003, MNRAS, 346, 1055

Kennicutt, Jr., R. C. 1998, ARA&A, 36, 189

Kewley, L. J., Groves, B., Kauffmann, G., & Heckman, T. 2006, MNRAS, 372, 961

Kido, D., Ioka, K., Hotokezaka, K., Inayoshi, K., & Irwin, C. M. 2025, arXiv e-prints, arXiv:2505.06965

Kormendy, J. & Ho, L. C. 2013, ARA&A, 51, 511

Lambrides, E. L., Chiaberge, M., Heckman, T., et al. 2020, ApJ, 897, 160

Lansbury, G. B., Banerji, M., Fabian, A. C., & Temple, M. J. 2020, MNRAS, 495, 2652

Lanzuisi, G., Delvecchio, I., Berta, S., et al. 2017, A&A, 602, A123

Law, D. R., E. Morrison, J., Argyriou, I., et al. 2023, AJ, 166, 45

Leighly, K. M., Halpern, J. P., Jenkins, E. B., & Casebeer, D. 2007, ApJS, 173, 1

Liu, Q., Narayanan, D., & Davé, R. 2019, MNRAS, 490, 1425

Liu, G., Zakamska, N. L., & Greene, J. E. 2014, MNRAS, 442, 1303

Liu, T., Tozzi, P., Wang, J.-X., et al. 2017, ApJS, 232, 8

Liu, W., Fan, X., Yang, J., et al. 2024, ApJ, 976, 33

Lodieu, N., Pinfield, D. J., Leggett, S. K., et al. 2007, MNRAS, 379, 1423

Loiacono, F., Decarli, R., Mignoli, M., et al. 2024, A&A, 685, A121

Luo, B., Brandt, W. N., Hall, P. B., et al. 2015, ApJ, 805, 122

Lupi, A., Quadri, G., Volonteri, M., Colpi, M., & Regan, J. A. 2024a, A&A, 686, A256

Lupi, A., Trinca, A., Volonteri, M., Dotti, M., & Mazzucchelli, C. 2024b, A&A, 689, A128

Luridiana, V., Morisset, C., & Shaw, R. A. 2015, A&A, 573, A42

Lusso, E., Comastri, A., Vignali, C., et al. 2010, A&A, 512, A34

Lyke, B. W., Higley, A. N., McLane, J. N., et al. 2020, ApJS, 250, 8

Madau, P. & Haardt, F. 2024, ApJ, 976, L24

Magorrian, J., Tremaine, S., Richstone, D., et al. 1998, AJ, 115, 2285

Maiolino, R. & Rieke, G. H. 1995, ApJ, 454, 95

Marcotulli, L., Connor, T., Bañados, E., et al. 2025, ApJ, 979, L6

Marshall, M. A., Perna, M., Willott, C. J., et al. 2023, A&A, 678, A191

Marshall, M. A., Yue, M., Eilers, A.-C., et al. 2024, arXiv e-prints, arXiv:2410.11035

Martínez-Aldama, M. L., del Olmo, A., Marziani, P., et al. 2018, A&A, 618, A179

Marziani, P., Dultzin, D., Sulentic, J. W., et al. 2018, Frontiers in Astronomy and Space Sciences, 5, 6

Marziani, P., Sulentic, J. W., Zwitter, T., Dultzin-Hacyan, D., & Calvani, M. 2001, ApJ, 558, 553

Matsuoka, Y., Iwasawa, K., Onoue, M., et al. 2022, ApJS, 259, 18

Matsuoka, Y., Iwasawa, K., Onoue, M., et al. 2025, ApJS, 280, 68

Matsuoka, Y., Iwasawa, K., Onoue, M., et al. 2019, ApJ, 883, 183

Matsuoka, Y., Iwasawa, K., Onoue, M., et al. 2018a, ApJS, 237, 5

Matsuoka, Y., Onoue, M., Iwasawa, K., et al. 2023, ApJ, 949, L42

Matsuoka, Y., Onoue, M., Kashikawa, N., et al. 2018b, PASJ, 70, S35

Matsuoka, Y., Onoue, M., Kashikawa, N., et al. 2016, ApJ, 828, 26

Mazzolari, G., Übler, H., Maiolino, R., et al. 2024, A&A, 691, A345

Mazzucchelli, C., Bischetti, M., D'Odorico, V., et al. 2023, A&A, 676, A71

Mechtley, M., Windhorst, R. A., Ryan, R. E., et al. 2012, ApJ, 756, L38

Miller, J. M. 2007, ARA&A, 45, 441

Morisset, C. 2013, pyCloudy: Tools to manage astronomical Cloudy photoionization code, Astrophysics Source Code Library, record ascl:1304.020

Mortlock, D. J., Patel, M., Warren, S. J., et al. 2009, A&A, 505, 97

Mortlock, D. J., Warren, S. J., Venemans, B. P., et al. 2011, Nature, 474, 616

Murray, N., Chiang, J., Grossman, S. A., & Voit, G. M. 1995, ApJ, 451, 498

Nagao, T., Maiolino, R., & Marconi, A. 2006, A&A, 447, 863

Naidu, R. P., Matthee, J., Katz, H., et al. 2025, arXiv e-prints, arXiv:2503.16596

Nanni, R., Vignali, C., Gilli, R., Moretti, A., & Brandt, W. N. 2017, A&A, 603, A128

Netzer, H. 2015, ARA&A, 53, 365

Netzer, H., Shemmer, O., Maiolino, R., et al. 2004, ApJ, 614, 558

Ni, Q., Brandt, W. N., Luo, B., et al. 2022, MNRAS, 511, 5251

Ni, Q., Brandt, W. N., Luo, B., et al. 2018, MNRAS, 480, 5184

Ni, Y., Di Matteo, T., Gilli, R., et al. 2020, MNRAS, 495, 2135

Nicholls, D. C., Sutherland, R. S., Dopita, M. A., Kewley, L. J., & Groves, B. A. 2017, MNRAS, 466, 4403

Nikolajuk, M. & Walter, R. 2012, MNRAS, 420, 2518

Onoue, M., Kashikawa, N., Matsuoka, Y., et al. 2019, ApJ, 880, 77

Osterbrock, D. E. & Ferland, G. J. 2006, Astrophysics of gaseous nebulae and active galactic nuclei

Osterbrock, D. E. & Pogge, R. W. 1985, ApJ, 297, 166

Park, D., Barth, A. J., Ho, L. C., & Laor, A. 2022, ApJS, 258, 38

Peca, A., Cappelluti, N., Urry, C. M., et al. 2023, ApJ, 943, 162

Perna, M., Arribas, S., Marshall, M., et al. 2023, A&A, 679, A89

Peterson, B. 2006, The Broad-Line Region in Active Galactic Nuclei, ed. D. Alloin, R. Johnson, & P. Lira (Berlin, Heidelberg: Springer Berlin Heidelberg), 77–100

Plotkin, R. M., Shemmer, O., Trakhtenbrot, B., et al. 2015, ApJ, 805, 123

Pu, X., Luo, B., Brandt, W. N., et al. 2020, ApJ, 900, 141

Pudoko, M., Wang, F., Fan, X., et al. 2025, arXiv e-prints, arXiv:2505.07932

Quadri, G., Trinca, A., Lupi, A., Colpi, M., & Volonteri, M. 2025, arXiv e-prints, arXiv:2505.05556

Reed, S. L., McMahon, R. G., Banerji, M., et al. 2015, MNRAS, 454, 3952

Reines, A. E. & Volonteri, M. 2015, ApJ, 813, 82

Ren, W., Guo, H., Shen, Y., et al. 2024, ApJ, 974, 153

Richards, G. T., Lacy, M., Storrie-Lombardi, L. J., et al. 2006, ApJS, 166, 470

Rieke, M. J., Kelly, D. M., Misselt, K., et al. 2023, PASP, 135, 028001

Rivera, A. B., Richards, G. T., Gallagher, S. C., et al. 2022, ApJ, 931, 154

Rivera, A. B., Richards, G. T., Hewett, P. C., & Rankine, A. L. 2020, ApJ, 899, 96

Rupke, D. S. N. 2014, IFSFIT: Spectral Fitting for Integral Field Spectrographs

Rupke, D. S. N. & Schweitzer, M., Viola, V., et al. 2021, QUESTFIT: Fitter for mid-infrared galaxy spectra

Rupke, D. S. N. & Veilleux, S. 2013, ApJ, 768, 75

Rusakov, V., Watson, D., Nikopoulos, G. P., et al. 2025, arXiv e-prints, arXiv:2503.16595

Schindler, J.-T., Bañados, E., Connor, T., et al. 2023, ApJ, 943, 67

Schmitt, H. R., Donley, J. L., Antonucci, R. R. J., et al. 2003, ApJ, 597, 768

Scholtz, J., Maiolino, R., D'Eugenio, F., et al. 2025, A&A, 697, A175

Scoville, N., Lee, N., Vanden Bout, P., et al. 2017, *ApJ*, 837, 150

Shemmer, O., Trakhtenbrot, B., Anderson, S. F., et al. 2010, *ApJ*, 722, L152

Shen, Y., Grier, C. J., Horne, K., et al. 2024, *ApJS*, 272, 26

Shen, Y. & Ho, L. C. 2014, *Nature*, 513, 210

Shen, Y., Wu, J., Jiang, L., et al. 2019, *ApJ*, 873, 35

Stanway, E. R. & Eldridge, J. J. 2018, *MNRAS*, 479, 75

Steffen, A. T., Strateva, I., Brandt, W. N., et al. 2006, *AJ*, 131, 2826

Stern, J., Behar, E., Laor, A., Baskin, A., & Holczer, T. 2014a, *MNRAS*, 445, 3011

Stern, J., Faucher-Giguère, C.-A., Zakamska, N. L., & Hennawi, J. F. 2016, *ApJ*, 819, 130

Stern, J. & Laor, A. 2013, *MNRAS*, 431, 836

Stern, J., Laor, A., & Baskin, A. 2014b, *MNRAS*, 438, 901

Stone, H., Orchard, M., Chang, E.-C., & Martucci, S. 2001, *Geoscience and Remote Sensing, IEEE Transactions on*, 39, 2235

Stone, M. A., Lyu, J., Rieke, G. H., & Alberts, S. 2023, *ApJ*, 953, 180

Storey, P. J. & Zeippen, C. J. 2000, *MNRAS*, 312, 813

Sulentic, J. W., Zwitter, T., Marziani, P., & Dultzin-Hacyan, D. 2000, *ApJ*, 536, L5

Tacconi, L. J., Genzel, R., Saintonge, A., et al. 2018, *ApJ*, 853, 179

Temple, M. J., Banerji, M., Hewett, P. C., et al. 2019, *MNRAS*, 487, 2594

Timlin, John D., I., Brandt, W. N., Zhu, S., et al. 2020, *MNRAS*, 498, 4033

Trefoloni, B., Carniani, S., Bertola, E., et al. 2025, *arXiv e-prints*, arXiv:2509.07064

Übler, H., Maiolino, R., Pérez-González, P. G., et al. 2024, *MNRAS*, 531, 355

Urry, C. M. & Padovani, P. 1995, *PASP*, 107, 803

Vayner, A., Díaz-Santos, T., Eisenhardt, P. R. M., et al. 2025, *ApJ*, 989, 230

Vayner, A., Zakamska, N. L., Ishikawa, Y., et al. 2024, *ApJ*, 960, 126

Ďurovčíková, D., Eilers, A.-C., Ishikawa, Y., et al. 2025, *arXiv e-prints*, arXiv:2510.09753

Veilleux, S., Liu, W., Vayner, A., et al. 2023, *ApJ*, 953, 56

Veilleux, S. & Osterbrock, D. E. 1987, *ApJS*, 63, 295

Vestergaard, M. & Osmer, P. S. 2009, *ApJ*, 699, 800

Vestergaard, M. & Peterson, B. M. 2006, *ApJ*, 641, 689

Vietri, G., Piconcelli, E., Bischetti, M., et al. 2018, *A&A*, 617, A81

Vito, F., Brandt, W. N., Bauer, F. E., et al. 2019a, *A&A*, 630, A118

Vito, F., Brandt, W. N., Bauer, F. E., et al. 2019b, *A&A*, 628, L6

Vito, F., Brandt, W. N., Yang, G., et al. 2018, *MNRAS*, 473, 2378

Volonteri, M. & Begelman, M. C. 2010, *MNRAS*, 409, 1022

Wang, B., Ishikawa, Y., Hennawi, J. F., et al. 2025, *arXiv e-prints*, arXiv:2508.02792

Wang, F., Fan, X., Yang, J., et al. 2017, *ApJ*, 839, 27

Wang, F., Yang, J., Fan, X., et al. 2021, *ApJ*, 907, L1

Wang, J.-M., Qiu, J., Du, P., & Ho, L. C. 2014, *ApJ*, 797, 65

Wolf, J., Salvato, M., Belladitta, S., et al. 2024, *A&A*, 691, A30

Wolf, J., Salvato, M., Coffey, D., et al. 2020, *MNRAS*, 492, 3580

Wu, J., Brandt, W. N., Hall, P. B., et al. 2011, *ApJ*, 736, 28

Wu, Q. & Shen, Y. 2022, *ApJS*, 263, 42

Wu, X.-B., Wang, F., Fan, X., et al. 2015, *Nature*, 518, 512

Wylezalek, D., Vayner, A., Rupke, D. S. N., et al. 2022, *ApJ*, 940, L7

Yang, J., Wang, F., Fan, X., et al. 2021, *ApJ*, 923, 262

Yang, J., Wang, F., Fan, X., et al. 2020, *ApJ*, 897, L14

Yi, W., Vivek, M., Brandt, W. N., et al. 2019, *ApJ*, 870, L25

York, D. G., Adelman, J., Anderson, John E., J., et al. 2000, *AJ*, 120, 1579

Yue, M., Eilers, A.-C., Simcoe, R. A., et al. 2024, *ApJ*, 966, 176

Zakamska, N. L., Hamann, F., Páris, I., et al. 2016, *MNRAS*, 459, 3144

Zhang, K., Wang, T.-G., Gaskell, C. M., & Dong, X.-B. 2013, *ApJ*, 762, 51

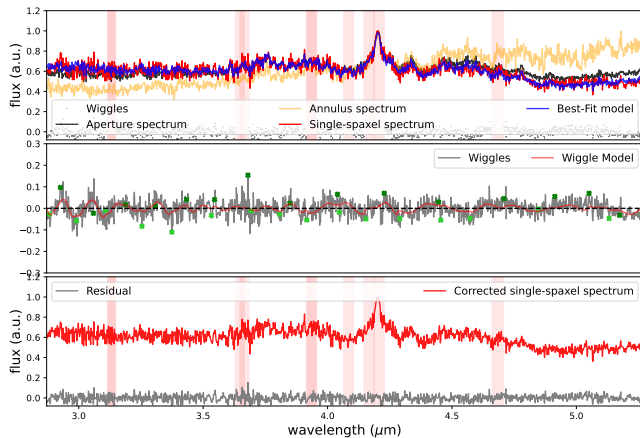


Fig. A.1. Correction of the brightest pixel of J0313-1806 using **WICKED**. *Top*: The solid red line shows the brightest spaxel spectrum of J0313-1806, fitted using a combination of an aperture and annular integrated spectra (black and yellow lines) templates, a power-law and a 2nd-degree polynomial, and shown in blue. Red vertical lines indicate masked regions of known emission lines excluded from the fit. The gray dots display the residuals. *Middle*: The wiggle spectrum is shown in gray and the best-fit wiggle model in red. The green X's are the peaks and valleys of the wiggles spectrum used to divide the wiggle spectrum to constrain its model shown in red (see Dumont et al. (2025) for details). *Bottom*: In red is shown the wiggle-corrected spectrum, and the residuals in gray.

Appendix A: Post-processing PSF undersampling with **WICKED**

Both IFU units of JWST, in particular NIRSpec, are spatially undersampled without reaching Nyquist sampling at any wavelength (Law et al. 2023). While our dithering strategy partially addresses this issue, we still visually detect sinusoidal modulations or *wiggles* produced by undersampled PSF, as observed in other Quasar data (e.g. Perna et al. 2023; Liu et al. 2024). These instrumental artifacts can significantly impact the shape of the continuum and emission lines in the spectrum. We use the PYTHON package **WICKED** to remove the *wiggle* from the spectrum, described in more detail in Dumont et al. (2025). **WICKED** uses an aperture and annular integrated spectra templates, a power law, and a second-degree polynomial to model the spectrum. This model represents a *wiggle* free model of the spectrum, which is used to create a *wiggle* spectrum by subtracting this model from the spectrum. This *wiggle* spectrum is then fitted with a series of sinusoidal fits and then removed from the spectrum. Figure A.1 shows an example of **WICKED** for the removal of *wiggle* from the brightest cube pixel spectrum of J0313-1806 (red).

We used a five-spaxel aperture spectrum template (black) and an eight-spaxel annular template (yellow), which are used in **WICKED** to create the best-fit model shown in blue. In the middle panel, the best-fit wiggle model is shown in red, and in the bottom panel, the corrected spectrum is shown in red. We ran **WICKED** with default parameters and a frequency prior of $8 \mu\text{m}^{-1}$ which leads to a better fit for the wiggle model. We set `SMOOTH_SPECTRUM` to "yes" during the flagging of spaxels with wiggles. This applies a $0.01 \mu\text{m}$ mean smoothing to the spectrum, which improves the detection of wiggles in low signal-to-noise data. We used a 3.5σ Fourier ratio in **WICKED**, leading to 103 spaxels in the datacube flagged as affected by wiggles.

Figure A.2 shows the comparison between a 3-spaxel ($\sim 3 \times \text{FWHM}$) aperture extraction between the corrected with

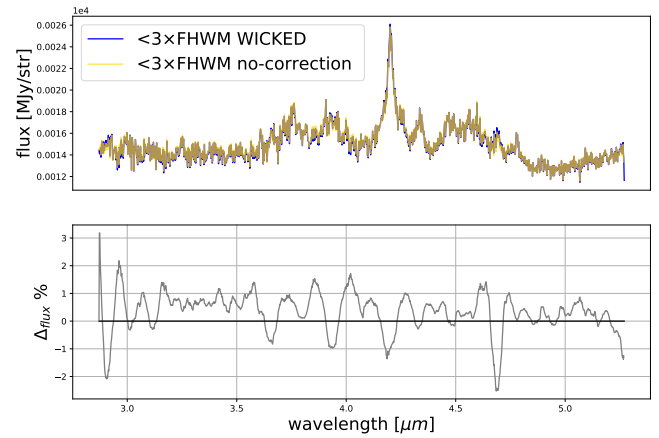


Fig. A.2. *Top*: 3-spaxel aperture spectrum comparison for the datacube corrected with **WICKED** (blue) vs. uncorrected (yellow). *Bottom*: Percentage difference (grey) between the uncorrected and **WICKED** data.

WICKED and the original datacube. We observe a mean difference of $\sim 0.3\%$ and a maximum difference of $\sim 2\%$. This is within the difference $\leq 5\%$ for the corrected vs. uncorrected data described in Dumont et al. (2025).

Appendix B: Determination of quasar spectrum extraction radius

In Fig. B.1 we show the wavelength-dependent flux fractions of the nuclear spectra extracted with apertures in the range 3–14 pixels, $0''.15$ – $0''.70$, relative to that obtained with a larger reference aperture of radius 20 pixels, i.e. $1''.0$. For smaller apertures, the downturn toward longer wavelengths reflects the fact that the PSF broadens with increasing wavelength, so a fixed aperture encloses a decreasing fraction of the total flux. Based on this figure, we adopted an extraction aperture with a radius of $0''.35$.

Appendix C: Tentative detection of extended continuum emission

After the line and continuum fitting procedure, we searched for significant continuum emission: we searched for contiguous regions of at least 5 spaxels for which the mean continuum in the spectral window $\delta\lambda = 3 - 4.2 \mu\text{m}$ is at least detected at the 1σ level. We confirm the detection of an elliptical nebula to the north-east of the quasar position. The relative positions of this low-surface brightness ellipse and the $\text{H}\beta$ line emitting region are shown in Fig. C.1. We fitted a Sérsic profile to this continuum detected nebula. Its centroid is constrained to $x_{\text{pix}} = 44$ and $y_{\text{pix}} = 47$. We further find an ellipticity of 0.39 ± 0.01 , a Sérsic index of $n = 0.51 \pm 0.02$ and an effective radius of $r_e = 7.05 \pm 0.10 \text{ pix}$. Assuming this structure is at the quasar redshift $z = 7.6423$, the effective radius corresponds to a physical scale of $1.75 \pm 0.02 \text{ kpc}$. The diffuse continuum emission could potentially trace a compact, moderately flattened companion of the quasar, with a shallow surface brightness profile typical of disturbed disks, tidal debris, irregular galaxies. This is further supported by the large offset between the quasar and the centre of the ellipsoid of $\sim 1.2 \text{ kpc}$ and the distinct morphologies of the $\text{H}\beta$ line-emitting envelope and the smooth-profiled and symmetric detected continuum. The large dispersion in the $\text{H}\beta$ shell further suggests velocity shear, a typical feature of interactions.

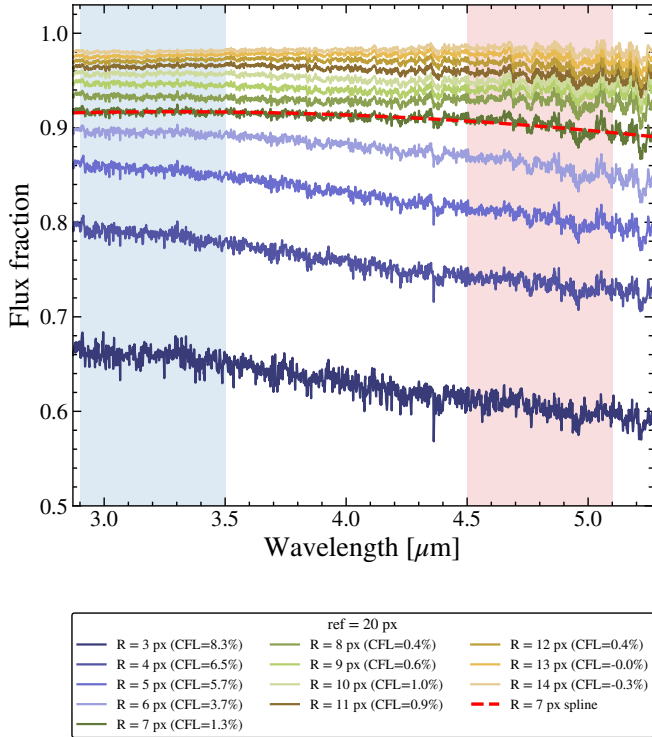


Fig. B.1. Wavelength-dependent encircled-flux fractions for different aperture radii, shown relative to a large reference aperture of $1\farcs0$. The legend reports the corresponding chromatic flux losses as defined in the main text. A 7-pixel radius achieves percent-level chromatic flux loss while avoiding the increased background and extended-emission contamination present in larger apertures. The spline function fitted to the 7-pixel curve is shown as a red dashed line. The blue and red bands correspond to the regions we compute the chromatic flux losses from: $(2.9\text{--}3.5\,\mu\text{m})$ and $(4.5\text{--}5.1\,\mu\text{m})$.

Given the absence of clear, distinctive spectral features to identify the redshift of this potential companion, we cannot exclude that it is located in the fore- or background. As most massive quasar hosts are expected to be compact and anchored in deep gravitational potentials, it is unlikely that the continuum corresponds to an irregular extension of the quasar's host galaxy. Furthermore, many high-redshift quasars observed with JWST/NIRSpec IFU so far appear to find themselves in some kind of interaction with a companion galaxy (e.g, Marshall et al. 2024; Decarli et al. 2024).

Appendix D: Spectra extracted from various emission regions in the NIRSpec IFU cube of J0313–1806

In Fig. D.1 we display spectra extracted within $0\farcs35$ of regions A, B and C defined in Section 4.1.

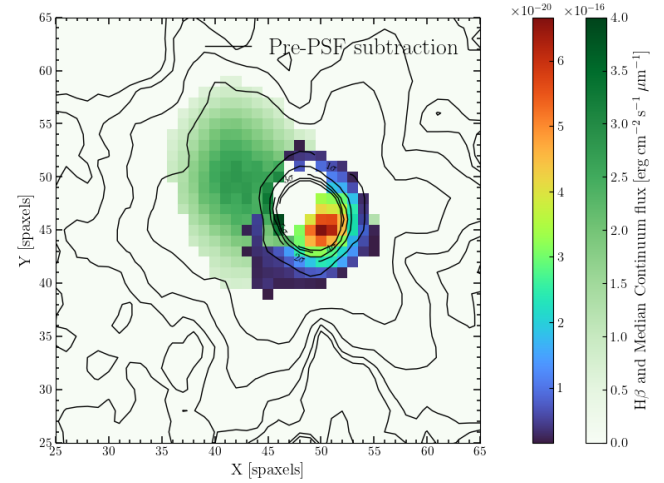


Fig. C.1. Median continuum in PSF-subtracted cube. The green coloured region corresponds to all islands of at least 5 contiguous spaxels with a mean continuum, measured over $3\text{--}4.2\,\mu\text{m}$, detected at the 1σ level. We compare it here to the contours of the initial non-PSF-subtracted quasar cube. We also indicate the location of the significant $\text{H}\beta$ line emission envelope. The offset location of the continuum emission and its elliptical morphology indicate that it is likely not a PSF residual.

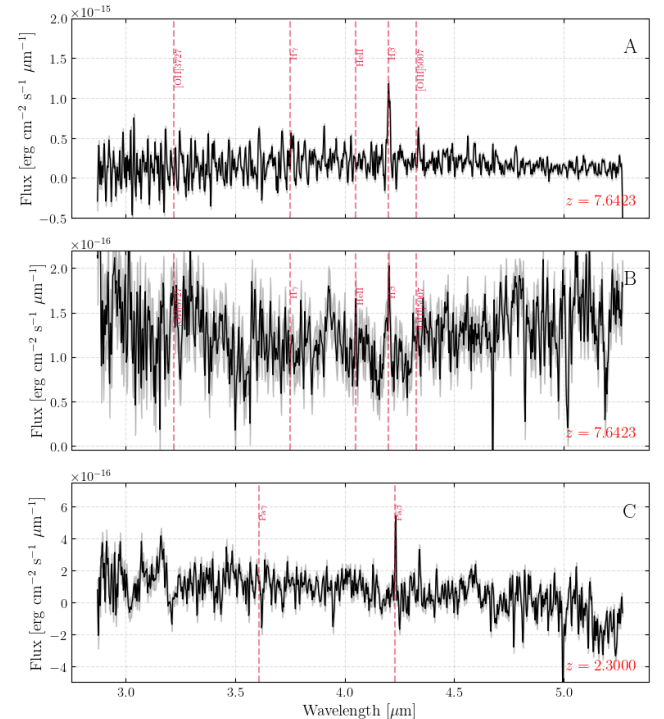


Fig. D.1. Spectra extracted from the PSF-subtracted NIRSpec IFU cube within circular apertures of radii $0\farcs35$ at the regions A, B and C (defined in Section 4.1). Region A corresponds to the $\text{H}\beta$ nebula discussed in this paper. Region B corresponds to the extended continuum emission around to the north-east of the quasar. Region C corresponds to a foreground galaxy at $z = 2.3$.